ESTABLISHING AND OPTIMIZING A PIPELINE FOR USING A COMBINED MULTI-OMIC APPROACH TO ASSESSING THE ROLE OF EIF5B IN GLIOBLASTOMA CELLS

KEIRAN JOHN VANDEN DUNGEN
Bachelor of Science, University of Lethbridge, 2018

A thesis submitted
in partial fulfilment of the requirements for the degree of

MASTER OF SCIENCE

in

BIOCHEMISTRY

Department of Chemistry and Biochemistry
University of Lethbridge
LETHBRIDGE, ALBERTA, CANADA

ESTABLISHING AND OPTIMIZING A PIPELINE FOR USING A COMBINED MULTI-OMIC APPROACH TO ASSESSING THE ROLE OF EIF5B IN GLIOBLASTOMA CELLS

KEIRAN VANDEN DUNGEN

Date of Defense: December 3, 2020

Dr. Nehal Thakor Thesis Supervisor	Associate Professor	Ph.D.
Dr. Athanasios Zovoilis Thesis Examination Committee Member	Assistant Professor	Ph.D.
Dr. Igor Kovalchuk Thesis Examination Committee Member	Professor	Ph.D.
Dr. Steven Mosimann Chair, Thesis Examination Committee	Associate Professor	Ph.D.

DEDICATION

To my loving partner Stephanie, who inspired me, motivated me, and pushed me to do the best I could. These last few years have been the best of times, made even better with you by my side.

ABSTRACT

Translation is an important and highly regulated process. Specifically, translation initiation is of interest when considering the ways in which cells respond to treatments and environmental changes. Previously, we demonstrated that eIF5B is responsible for the translation of a subset of mRNAs encoding anti-apoptotic proteins which regulated the sensitivity of U343's resistance to TRAIL. Through this project, I have established an important multi-omics pipeline for investigating the impact of eIF5B on glioblastoma cells. By utilizing this pipeline, I have demonstrated that both TRAIL and eIF5B individually affected the glioblastoma cell metabolome, and in combination revealed further changes. Specifically, these treatment conditions produced robust shifts in metabolites such as *myo*-inositol. I have successfully prepared sequencing-ready RNA libraries for Ribo-seq with corresponding RNA for RNA-seq. This research will provide our lab the opportunity to expand my research on eIF5B through this pipeline as I have demonstrated that eIF5B-modulated metabolites are very cancer-relevant.

ACKNOWLEDGEMENTS

First, I would like to thank Dr. Nehal Thakor. As a supervisor, he motivated me to push myself every day, provided me with countless opportunities, offered continual guidance, and helped me to establish valuable connections that greatly increased the quality of my work. I would also like to thank my committee members Drs. Athan Zovoilis and Igor Kovalchuk for their valuable input and offered time. I would also like to thank Dr. Mehdi Jafarnejad as a collaborator for all his assistance and advice. Additionally, I would like to thank each member of the Thakor lab for their guidance, mentorship, friendship, and continued motivation. Thank you to Kamiko, Keith, Jean Claude, Joe, Rachana, each undergraduate student in the lab, and all previous members for all their support, laughter, and general shenanigans. You all really made the last few years and any time spent in lab a great enjoyment filled with laughter and long hours. Next, I would like to thank Josh, Tony, and the Montina lab for all the time and assistance they put towards this project. Without their assistance, much of this project would not be possible. I would also like to thank David for always being around and offering continuing advice. Late night experiments just would not have been the same without you there! Finally, I would like to thank my family and friends for their support, advice, and constant motivation. Special thanks to my loving partner Stephanie; without her constant motivation and emotional support during the last 6 years, and specifically over the last few months, this thesis (and subsequently my mental health) would have been vastly different – and for the worse.

TABLE OF CONTENTS

LIST OF TABLES

LIST OF FIGURES

LIST OF ABBREVIATIONS

A-II	grade II astrocytoma
APAF-1	apoptotic protease-activating factor 1
ASS1	arginosuccinate synthase
ATF4	activating transcription factor 4
Bcl-2	B cell lymphoma 2
Bcl-xL	B cell lymphoma extra long
BH3	Bcl-2 homology domain 3
caspase	cysteine aspartic protease
CCT	CTP:phosphocholine cytidyltransferase
CDP-Cho	cytidine diphosphate (CDP)-choline
c-FLIP	cellular FLICE-like inhibitor protein
CHK	choline kinase
CHKA	choline kinase α
CHX	cycloheximide
CI	confidence interval
cIAP	cellular inhibitor of apoptosis
CK	cytosolic Cr kinase
Ckmt1	mitochondrial creatine kinase 1
CTC	circulating tumor cells
DED	death effector domain
DISC	death-inducing signaling complex
DMEM	Dulbecco's Modified Eagle Medium
DR4/5	death receptors 4/5
DTT	1,4-dithiothreitol
EGFR	epidermal growth factor receptor
eIF	eukaryotic initiation factor
eIF4E-BP	eukaryotic initiation factor 4E binding protein
ERK	extracellular signal-regulated kinase
FasL	Fas ligand
FBS	fetal bovine serum
FH	fumarate hydratase
GBM	Glioblastoma
GPCho	glycerophosphocholine
GPCPD1	Glycerophosphocholine phosphodiesterase 1
HBP	hexosamine biosynthetic pathway
HER2	human epidermal growth factor receptor 2
HIF1α	hypoxia inducible factor 1 subunit alpha
IAP	inhibitor of apoptosis protein

IMPA	myo-inositol-1-monophosphatase
INO1	inositol-3-phosphate synthase 1
IP3	inositol triphosphate
IRES	internal ribosome entry site
ISR	integrated stress reponse
Keap1	Kelch like ECH associated protein 1
LDHA	lactate dehydrogenase 4
MI	myo-inositol
MOM	mitochondrial outer membrane
MS	mass spectrometry
MW	Mann-Whitney
NF-κB	nuclear factor kappa B
NMR	nuclear magnetic resonance
Nrf2	nuclear factor erythroid 2-related factor 2
NSCLC	nonsmall cell lung cancer
OGT	O-GlcNAc transferase
PABP	poly-A binding protein
PBS	phosphate buffered saline
PCA	principal component analysis
PCD	programmed cell death
PCho	phosphocholine
PCR	polymerase chain reaction
PD-L1	programmed death ligand 1
PH	plekstrin-homology domain
PI3K	phosphatidylinositol-4,5-bisphosphate 3-kinase
PIC	pre-initiation complex
PIP	phosphatidylinositol phosphate lipid
PIP3	phosphatidylinositol-3,4,5-triphosphate
PLA2	phosphatidylcholine-specific phospholipase
PTC	papillary thyroid carcinoma
PtdIns	phosphatidylinositol
PtdIns3P	phosphatidylinositol 3-phosphate
PTEN	phosphatase and tensin homolog
QC	quality control
qPCR	quantitative polymerase chain reaction
RFA	ribosome footprinting assay
Ribo-seq	ribosome profiling
RIPA	radioimmunoprecipitation buffer
ROS	reactive oxygen species
rRNA	ribosomal ribonucleic acid
RTK	receptor tyrosine kinase

SH2	src-homology domain
SHIP1	SH2 domain containing inositol polyphosphate 5-phosphatase 1
siRNA	small interfering ribonucleic acid
SMIT	sodium-dependent myo-inositol transporter
TC	ternary complex
tCho	total choline-containing compounds
TE	translation efficiency
TMZ	temozolomide
TNF	tumour necrosis factor
TRAIL	TNFα-related apoptosis-inducing ligand
tRNA	transfer ribonucleic acid
TSP	trimethylsilylpropranoic acid
UDP-GlcNAc	UDP-N-acetylglucosamine
uORF	upstream open reading frame
UTR	untranslated region
VEGFA	vascular endothelial growth factor A
XIAP	X-linked inhibitor of apoptosis protein

1 Introduction

1.1 Translation

Translation is the second step in protein synthesis, following transcription, and can be broken down into three primary steps: initiation, elongation, and termination. Of those, initiation is the most regulated, and therefore of interest when investigating rapid changes in protein expression.[1] Many factors such as cellular stress, apoptosis, and hypoxia affect the rate at which translation can occur; consequently, rapid changes in protein expression occur under these conditions of stress.[1,2]

While mRNA levels have traditionally been considered the gold-standard in observing expression changes, translation efficiency (TE) has become an often studied and very important part of the growing field of protein synthesis.[2,3] Notably, recent studies indicate that considering transcriptional changes alone does not provide enough information to accurately predict protein expression levels, indicating the importance of studying mRNA translation as a regulatory step in protein synthesis.[2,4] Translation is an energetically costly process; as a result, it is tightly regulated by various mechanisms. Under conditions of stress that would activate the integrated stress response (ISR), global translation becomes downregulated *via* phosphorylation of the eukaryotic initiation factor 2α (eIF2α) subunit which subsequently prevents eIF2 from effectively initiating translation.[5,6] Although canonical translation was traditionally believed to be fully inhibited under conditions of eIF2α phosphorylation, multiple alternative mechanisms have been discovered that allow for eIF2-independent translation initiation under both cap-dependent and cap-independent translation initiation.[3,7]

1.2 Canonical vs. Non canonical translation

While a highly regulated and complex process, eukaryotic translation initiation can be simplified into four primary components: formation of the pre-initiation complex (PIC), recruitment onto the mRNA, scanning for a start codon (AUG), and formation of the competent 80S ribosomal initiation complex. Canonical eukaryotic translation initiation requires more than 25 polypeptides and 13 eukaryotic initiation factors in order to successfully identify, scan, and initiate translation of an mRNA.[5] The small (40S) ribosomal subunit binds to the 5' m^7GpppN cap of an mRNA, initiating scanning in a 5' to 3' direction. Upon successfully identifying an AUG start codon, the large (60S) ribosomal subunit is recruited to the 40S subunit forming a full 80S ribosome capable of translation.

To start this process, a Ternary complex (TC) is formed, which is comprised of eIF2-GTP bound to the initiator Met-$tRNA_i$. The TC, along with the 40S PIC (eukaryotic initiation factors 3, 1, 1A, and 5), form the 43S PIC. Concurrently to this happening, an mRNA is activated by the binding of the eIF4F cap-binding complex to the 5' cap of the mRNA. The 43S PIC is recruited to the activated mRNA and scans along in a 5' to 3' direction until an AUG start codon is located.[6,8] The eIF4F complex is comprised of the cap-binding eIF4E, the helicase eIF4A, and the scaffold protein eIF4G. Previously believed to be crucial to translation initiation, even under conditions of internal ribosome entry site (IRES) cap-independent translation, eIF4G is not required in all circumstances.[7,9] Specifically, the XIAP IRES was translated in the absence of eIF4G in an eIF5B-dependent manner.[7] As a scaffold protein, eIF4G directly interacts with eIF4E – one of the only eIFs capable of directly binding the 5' cap, and poly-A binding protein (PABP).[3,6] This simultaneous reaction is believed to cause circularization of the mRNA, bringing the 3' UTR towards the 5' UTR.[3,10] Many regulatory elements exist in the 3' UTR of eukaryotic

mRNAs – including the uncommon 3' IRESs.[11] Under certain viral infections, eIF4G is cleaved by viral proteases to inhibit traditional cap-dependent translation.[12] As a result, while canonical eIF4G-dependent translation is decreased, alternative non-canonical translation initiation mechanisms still occur. Notably, both VEGFA and HIF1α are preferentially translated *via* their IRESs in breast cancer cells under hypoxic conditions.[12] This increase in non-canonical translation is believed to be at least in part due to increases in both eIF4G and eIF4E-BP which inhibits the activity of the cap-binding eIF4E.[12]

Once the scanning 43S PIC has located an AUG start codon, the complex is referred to as the 48S PIC. Upon binding of the initiator tRNA in the P site, eIF5 catalyzes the GTP hydrolysis of eIF2-GTP and subsequent release of eIF2-GDP, a release which is necessary for eIF5B-catalyzed recruitment and joining of the 60S subunit to create a functional 80S ribosome.[13] eIF5B has also been shown to play an important alternate role in cap-independent IRES-mediated translation initiation.[7,14] In mammalian cell lines, eIF5B has been shown to play a specific role in the alternative delivery of met-tRNAi for translation initiation on the X-linked inhibitor of apoptosis protein (XIAP) IRES element.[7] This alternate delivery mechanism was observed under conditions of eIF2α phosphorylation which causes a functional inhibition of eIF2. Induction of the ISR, hypoxia, ER stress, and apoptosis are just a few of the many environmental stress conditions which can result in the phosphorylation eIF2α.[5,15] Conditions such as these are of special interest when considering cancer cells as they frequently experience many of these environmental stresses regularly and still effectively synthesize new proteins to facilitate growth and survival.[6] Many cancers rely on alternative mechanisms of translation as a requirement to survive, whether by translating pro-growth genes, or simply by increasing production of pro-

survival proteins such as IAPs. Through the regulation of multiple IAPs and anti-apoptotic proteins, eIF5B plays an important role in cancer cell survival and apoptosis avoidance.[7,15]

1.3 Apoptosis

Apoptosis is an ATP-dependent form of programmed cell death (PCD) driven by cysteine-dependent aspartate-driven proteases (Caspases). Classically, cell death was thought to exist in two primary forms: necrosis (uncontrolled and ATP-independent) and apoptosis.[16] However, in recent years alternative forms of PCD such as necroptosis, ferroptosis, and autophagy have been discovered.[17-19] Traditional characteristics of apoptosis include membrane blebbing, chromatin condensation, nuclear DNA fragmentation, caspase activation, and the flipping of phosphatidylserine to the exterior of the cell membrane. While classical apoptosis includes each of these characteristics, alternative forms of PCD may show some, but not all these characteristics. These alternative forms of PCD may differ in activation or may differ in the method of execution. One such example is necroptosis: often referred to as programmed necrosis, necroptosis is activated by TNF binding to a death receptor but does not require downstream executioner caspases to cause cell death.[17,20,21]

There are three typical forms of apoptosis which differ in the activation and converge on the execution – extrinsic (death-receptor mediated), intrinsic (driven by cellular stress such as DNA damage), and granzyme B pathway (driven by granzyme B). While these different forms of apoptosis differ on how they initiate apoptosis, they are all caspase-dependent and converge at the point of mitochondrial membrane depolarization.[22] Mitochondrial release of cytochrome-c creates the apoptosome, resulting in the activation

of caspase-9, which ultimately cleaves caspase-3, the major executor of apoptosis.[23] In the case of apoptosis, this process is typically referred to as the caspase-cascade, resulting in cellular disassembly and DNA fragmentation.[24]

Caspases related to apoptosis can be broken down into two primary categories: the initiator (or apical) caspases, and the executioner (effector) caspases.[23,25] There is, however, a third category of caspases not related to apoptosis: the inflammatory caspases which contain caspases-1, -4, -5, and -12 (caspase-12 is only expressed in come humans). There are 7 caspases involved in apoptosis in humans: caspases-2, -8, -9, and -10 make up the apical caspases, and -3, -6, and -7 make up the executioner caspases.[26]

Extrinsic apoptosis is also referred to as receptor-mediated apoptosis due to its mode of activation – binding of a ligand to a death receptor. For extrinsic apoptosis to begin, a pro-apoptotic ligand binds to a death receptor and initiates the caspase cascade. One of the dominant families of proteins responsible for activating extrinsic apoptosis is the tumor necrosis factor (TNF) superfamily which includes notable members such as tumor necrosis factor alpha (TNFα), Fas ligand (FasL), and TNFα-related apoptosis-inducing ligand (TRAIL, also called APO2L).[24,27] Of these cytokines, TRAIL has been studied for its anti-cancer properties over recent years because TRAIL binds to the death receptors DR4 and DR5, initiating apoptosis in a variety of cancer cell lines, but not in healthy cells.[25,28,29] Once an apoptosis-inducing ligand has bound to a death receptor such as DR4/5, Fas-associated protein with death domain (FADD) is recruited to the death receptor and acts as bridge to connect the death receptor to the death effector domain (DED) of procaspase-8/10.[27] This complex, referred to as the death-inducing signaling complex (DISC), formation results in proteolytic self-cleavage of procaspase 8 to a functional caspase-8.[28] In turn, caspase-8 is able to activate apoptosis *via* two distinct mechanisms:

firstly, caspase-8 is able to directly cleave and activate the executioner caspase-3, secondly, caspase-8 cleaves the BH3-only protein Bid into its functional form, truncated Bid (tBid).[23,25,28,30]

Bid is a member of the proapoptotic BH3-only family of proteins, a subgroup of the Bcl-2 family, which includes Bid, Bim, Puma, Noxa, Bad, Bik, Bmf, and Hrk.[31] Most notably, BH3-only proteins such as Bid do not directly act on the mitochondria to induce apoptosis, but instead binds tightly to the BH3 domains of other Bcl-2 proteins to modify their activity. In total, there are three subgroups of the Bcl-2 family of proteins: (i) the pro-apoptotic proteins Bax and Bak, (ii) the anti-apoptotic Bcl-2 proteins like Bcl-xL, Bcl-2, and Mcl-1, and (iii) pro-apoptotic BH3-only proteins. The first group, the pro-apoptotic proteins including Bax and Bak, act on the mitochondrial outer membrane (MOM) to form pores known as MOM permeabilization.[28] This permeabilization allows for the release of multiple apoptosis-inducing proteins such as cytochrome c and SMAC/Diablo. The second group, the pro-survival Bcl-2 proteins such as Bcl-xL and Bcl-2 localize near the outer membrane of the mitochondria and are capable of interacting with other BH3-domain containing proteins such as Bax or Bid.[31] By interacting with Bax or Bak, the Bcl-xL / Bax interaction prevents Bax from effectively poring the MOM, resulting in an inhibition of Bax. The third group of Bcl-2 proteins, the pro-apoptotic BH3-only proteins, act on MOM permeabilization in two distinct ways. In the first way, active tBid is able to interact with the BH3 domain of Bax / Bak to permealize the MOM, resulting in release of cytochrome c.[28] On the other hand, BH3-only proteins are also able to bind to and inhibit pro-survival Bcl-2 proteins.[31] Since Bcl-xL and Bcl-2 would normally inhibit the activity of Bax / Bak, this inhibition by Bid effectively leaves Bax / Bak free to interact with a separate BH3-only protein and activate MOM permeabilization.

Just downstream of the mitochondria in the caspase cascade involves a multi-protein complex known as the apoptosome. Following cytochrome-c release from the mitochondria into the cytosol, it binds to and activates APAF-1, which triggers the formation of the apoptosome, a wheel-like structure made up of seven APAF-1-cytochrome-c proteins and seven pro-caspase-9 proteins on the exterior.[28,32] When fully formed, the apoptosome acts as a powerful apical caspase, with the activity of active caspase-9 to cleave and activate procaspase-3 and procaspase-7. Caspase-3 and caspase-7, as major executioners of apoptosis, are the final step in the caspase-cascade, effectively carrying out cell death.[23] There are, however, inhibitor of apoptosis proteins (IAP) that can inhibit the activity of caspase-9 and caspase-3 such as XIAP.[33] In addition to cytochrome-c release, the mitochondria frequently release SMAC / Diablo from the mitochondrial pores which inhibit these IAPs to assist in the promotion of apoptosis.

Intrinsic apoptosis, in contrast with extrinsic, does not require the activation of death-receptors on the cell membrane, but rather triggers from environmental stresses. These environmental stressors can include, but are not limited to DNA damage, ER stress, oxidative stress, or viral infection.[24] This stress typically acts on apoptosis in two complimentary ways: activation of Bax / Bak dimerization, and through upregulation of some BH3-only proteins such as Nox and Puma which bind to and inhibit the pro-survival Bcl-2 proteins.[24] The rest of apoptosis downstream of the mitochondria, however, is identical to that of extrinsic apoptosis in many cases, and only differs in its mechanism of initiating apoptosis.

There are many IAPs and anti-apoptotic proteins that inhibit different steps in the caspase-cascade of apoptosis, and some directly at the mitochondria (Bcl-xL, Bcl-2). Anti-apoptotic proteins play an important role in apoptosis regulation, and therefore are crucial

to tumor pathogenesis. Due to the fact that many drivers of cell division also trigger apoptosis as a regulatory mechanism, apoptosis defects arising alongside protooncogene greatly improve the success of a tumour.[34,35] Additionally, as a tumor grows, along with that growth comes increased oxidative stress, DNA errors, and chromosomal segregation errors – all of which would normally trigger apoptosis.[36] Hence, it is extremely important to the success of a cancer to increase expression of anti-apoptotic proteins. Notably, the important anti-apoptotic protein B-cell lymphoma 2 (Bcl-2) was originally discovered as an overexpressed protein in some B-cell lymphomas which played a crucial role in cancer survival.[37] Overexpression of many anti-apoptotic proteins such as the IAP family is upregulated in many cancers, and either Bcl-xl or Bcl-2 is believed to exist in over 50% of cancers.[38,39] Trends in expression of anti-apoptotic factors often lead to labelling certain cancer cell lines as resistant to some drug or other. Drug resistance to extrinsic apoptosis-inducing factors, such as TRAIL-resistance, can arise in several ways. This can occur because of changes in death receptor expression, or possibly due to changes in proteins involved in the caspase-cascade. Due to its reliance on DR4 / DR5 (also known as TRAIL receptor 1 and TRAIL receptor 2), some circulating tumor cells (CTCs) have been found to express a reduction in DR5 levels.[40] In other circumstances, increased expression of anti-apoptotic proteins such as cellular FLICE-like inhibitor protein (c-FLIP) are often associated with TRIAL-resistance. In nonsmall cell lung cancer (NSCLC), c-FLIP has been shown to play an essential role in TRAIL-resistance by directing the TRAIL-induced DISC formation towards activation of NF-κB and ERK cell signaling. In contrast, when c-FLIP was depleted or knocked down, DISC signaling once again induced apoptosis and removed the resistance to TRAIL.[38]

1.4 The Role of eIF5B in RNA Translation

Recently it has been shown that the eukaryotic initiation factor 5B (eIF5B) plays an important role in cell survival regulation through expression of many pro-survival proteins.[15] In the study, eIF5B is shown to promote the translation of XIAP, Bcl-xL, cIAP1, and c-FLIP$_S$. Depletion of eIF5B in glioblastoma multiforme cells resulted in sensitization to TRAIL-induced apoptosis *via* decreased expression of IAPs and pro-survival proteins.

Under standard conditions, eIF5B plays an important role in translation initiation by catalyzing the joining of the 40S and 60S ribosomal subunits. eIF5B is the eukaryotic homolog of the bacterial initiation factor 2 (IF2), the factor responsible for delivery of the initiator tRNA. However, while it does share sequence similarity, eIF5B does not, in canonical translation initiation, deliver the initiator tRNA in eukaryotes. Recent evidence, however, suggests that under specific conditions such as eIF2α phosphorylation, eIF5B is capable of IRES-driven delivery of the initiator tRNA in humans with the XIAP IRES.[7] More recently, eIF5B was shown to play an important role in facilitating met-tRNAi delivery under conditions of hypoxia sufficient for phosphorylating eIF2α.[5] Under these conditions, hypoxic cells were found to engage in cap-dependent translation using eIF4F^H, the hypoxic equivalent of eIF4F.[3] This complex was discovered to consist of eIF4E2, eIF4A, and eIF4G3 (functional homolog of eIF4G1) and demonstrated that both eIF4E2 and eIF4G3 were necessary for cap recognition and binding under hypoxic (1% O_2) conditions, but that depletion of them did not affect normoxic (21% O_2) cap-binding. Through the study, they separated genes into three distinct classes of TEs based on their relative expression under normoxic / hypoxic conditions, determining that while there was

classes that required either eIF4E or eIF4E2, there was also a class that was dependent on both eIF4E and eIF4E2. Under hypoxic conditions eIF5B was associated with $tRNAi^{Met}$ more frequently than under normoxic conditions; further, induction of a subset of hypoxia-response genes such as ATF4 was eIF5B-dependent and eIF2 independent. The authors conclude that eIF5B may directly deliver met-$tRNAi^{Met}$ and/or through ribosomal subunit joining.[5]

Multiple recent papers on the topic of eIF5B have been published over the last few years. Published in Nature Cancer, Suresh *et al* demonstrate the important role that eIF5B plays in the integrated stress response (ISR)-dependent translation of PD-L1; however, they also claim that eIF5B overexpression is sufficient to induce PD-L1 expression even without ISR activation.[41] The authors believe this mechanism to act by direct recruitment to the initiation site under conditions of eIF2α phosphorylation; in doing so, the inhibitory uORFs on the PD-L1 mRNA are avoided and increased PD-L1 translation occurs. This data supports the notion that not only is eIF5B plays an important role in translation under ISR-inducing conditions. Separately, two notable papers were published by Wang *et al* over the last year in Nature Letters and Nature Communications which delve deeper into mechanism behind eIF5B.[42,43] Taken together, these two publications explain that the GTPase activity of eIF5B is required to dissociate from the 80S ribosomal complex and therefore prevent the transition from translation initiation to elongation.[42] Further, in their more recent publication of the two, Wang *et al* investigates the structure of this interaction *via* CryoEM. Through this study, they make two primary claims: first, that unlike other tRNAs, Met-$tRNA_i^{Met}$ is capable of binding directly to the P site with the assistance and direction of eIF5B. Second, the authors show that the rate limiting step for the initiation-elongation transition is not GTP hydrolysis, but rather the dissociation of eIF5B-GDP.[43] Notably, both

of these papers used a yeast eIF5B (FUN12) which is approximately 25% smaller than the human eIF5B.

In humans, eIF5B plays an important role in assisting in the translation of specific subsets of genes under normoxic and hypoxic conditions. Specifically, under hypoxic conditions, eIF5B has been shown to play a crucial role in translation of genes in the central carbon metabolism, hypoxic adaptation, amino acid synthesis, cell adhesion, and endocytosis.[5] In my study, I wish to take the knowledge that eIF5B regulates specific metabolic pathways under hypoxic conditions and use this knowledge to investigate the role that eIF5B plays in survival and metabolic regulation.

1.5 Metabolomics

Metabolomics is the study of small molecules and metabolites in a living organism and is researched using two main techniques: nuclear magnetic resonance (NMR) spectroscopy, and with mass spectrometry (MS). Both techniques have pros and cons associated with them, and both are valid and currently used methods of studying small molecules in a living system. There are tens of thousands of known human metabolites, but of those, only around 1500 may be identified from global profiling, and in most situations, only a couple hundred at most can be identified. [44,45]

Alongside transcription and translation, the metabolome is greatly affected by environmental changes and stresses. The metabolome is made up of metabolites (small molecules < 1500 Da) which are downstream of transcriptomic and translatomic changes. These changes are rapid and reflect alterations in pathways, giving great insight into changes happening within a living organism. Metabolites can be collected from tissue or

fluid and give different results. Typically, biofluid metabolomics is frequently utilized because blood, urine, or other bodily fluids can be collected from living hosts. However, for small organisms and tissue culture, the analysis of tissue metabolomics reveals much information about significant changes in biochemical pathways which gives insight into how the organism is responding and adapting to stimuli.

Of the omics, metabolomics is often considered the closest to phenotype, and as a result, is very useful for studying mechanisms in cell culture to show an effect to specific environmental or treatment conditions.[46] For this reason, metabolomic data coinciding with translatomic / transcriptomic data could prove very useful for verifying that protein synthesis changes are reflected in the metabolome, therefore confirming which pathways were affected. Previously, metabolomic studies in cell culture have been used to study changes in the metabolome under conditions of stress such as hypoxia as well as silencing of specific genes such as NRF2.[47] siRNAs targeting initiation factors such as the eukaryotic initiation factor eIF5B have also been performed in cell culture in order to assess how pathways responded to hypoxic conditions in order to investigate and comment the role that eIF5B plays in translation of hypoxic-response genes. In contrast, in this experiment I perform a similar analysis to assess the role that eIF5B plays in apoptosis by using TRAIL as a mechanism to activate various pathways. Other authors have shown that apoptosis-inducing compounds can be used along with metabolomic data to comment on the mechanism of activity.[48] Using this idea in combination previous papers published in our lab on eIF5B and apoptosis, this will help elucidate the specific role that eIF5B is playing. In doing so, I can further investigate whether eIF5B acts through direct regulation of proteins involved in apoptosis, or indirectly *via* regulation of pathways involved.[48]

1.6 Translatomics

While transcriptomics taking a genome-wide snapshot of the abundance of mRNAs at a given time, translatomics is a method of examining global active translation of those mRNAs and thus present a robust tool in studying the changes in mRNA translation in response to various stimuli. One method of assessing translatomic activity which has become increasingly popular is through a process commonly referred to as Ribosome profiling (Ribo-seq), also referred to as ribosome footprinting assay (RFA).[49,50] Changes in mRNA concentrations notoriously disagree with protein expression, and Ribo-seq attempts to provide a more accurate assessment of the state of protein synthesis in a specific snapshot.[2,3] This is achieved by isolating ribosome-bound mRNA fragments and sequencing them in parallel with the total cytoplasmic mRNA population – in doing so, relative translation efficiencies (TE) can be calculated for any given mRNA, providing insight into translatomic regulation.

Ribosome profiling has many uses; however, in contrast with other popular techniques used to examine translation such as polysome profiling, ribosome profiling has both a few advantages as well as a few disadvantages.[49] On one hand, it provides information on global shifts in translation sequence-level ribosome-binding information; however, polysome profiling may still offer an advantage for analysis of transcript isoforms. Polysome profiling is the process of separating mRNAs based on the number of ribosomes bound to them. An mRNA with a with multiple bound ribosomes is referred to as a polysome – from this point they are typically sorted into mRNAs found in low MW polysome fractions, and high MW polysome fractions. These fractions are collected by density gradient separation of the ribosomes in sucrose and subsequent fractionation. In contrast, ribosome profiling provides information about protein synthesis by mapping

sequences of each bound ribosome. In order to achieve this, ribosomes are secured onto mRNAs *via* cycloheximide treatment, which blocks the elongation phase of mRNA translation, and then treated with RNAse I in order to isolate the ribosome protected footprints – that is, sequences which were being actively translated at the time of treatment. Following this, a library is prepared and sequenced so that the ribosome protected footprints can be quantified. Benefits of this technique involve information about the specific sequences where translation is occurring (positional information) in a nucleotide level resolution, information on translation initiation sites, and location of ribosome stalling.[49] Further, compared to polysome profiling, ribosome profiling provides a more accurate expression measurement because it provides exact data on the number of ribosomes present on a population of mRNAs, and does not require the approximate guesswork that polysome profiling requires. However, unlike ribosome profiling, polysome profiling provides information on the translation of entire transcripts, something that ribosome profiling lacks, and something that can be complimentary to the ribosome profiling data should they be performed together. Ingolia *et al* further notes that polysome profiling, in contrast with ribosome profiling, gives information on transcript-specific changes. In short, many genes have more than one mRNA transcript or splicing variants – by performing polysome profiling, it may be discovered that changes in translation are occurring on only one transcript or splice variant, and not uniformly across all transcripts for a gene.[49]

As a relatively new and constantly expanding field and technique, translation efficiency (TE) calculated *via* ribosome profiling is used for many different types of studies. TE is a measurement of translation changes for a gene relative to the abundance of their mRNA transcript. By gathering RNA-seq and Ribo-seq data from the same original sample, the total translation calculated from Ribo-seq can be standardized with its RNA-

seq data to calculate TE values for each gene. Recently, ribosome profiling has been used to examine TE changes that occur under specific treatment conditions such as hypoxia, conditions which would mimic EM-like transitions, and examination of the roles that specific genes play in upstream open reading frame (uORF) translation.[5,51,52] Here, I established a pipeline for assessing the role that eukaryotic initiation factors play in regulation of subsets of genes and their metabolomic pathways under conditions of apoptosis-inducing stress.

1.7 Hypothesis and Objective

I hypothesize that eIF5B depletion will result in large-scale metabolomic and translatomic shifts in many pathways including but not limited to cell survival and the central carbon metabolism. My research aims and objectives can be broken down into three primary goals. The first was to perform NMR-based metabolomics under both RNAi depletion of eIF5B as well as TRAIL treatment conditions in order to comment on global shifts in metabolomic expression. The second goal of this project was to develop, establish, and optimized a multi-omics pipeline to analyze shifts in global expression through across transcription, translation, and metabolomic pathways. The third and final goal of this thesis was to prepare sequencing-ready Ribo-seq libraries for U343 under conditions of eIF5B knockdown and TRAIL treatment in triplicate. By looking at these changes at multiple stages of expression, I want to begin the process of establishing eIF5B expression as an important indicator of tumour severity and response. Our previous publication supports the notion that eIF5B plays an important role in apoptosis pathways through regulation of multiple anti-apoptotic factors as well as key signaling pathways such as EGFR and NF-

κβ.[15] A recent publication exploring the role of eIF5B under hypoxic conditions demonstrated that, under hypoxic stress, eIF5B regulated a subset of hypoxic-specific genes, some of which were no regulated in an eIF5B-dependent manner in-dependent of an environmental effect such as hypoxia. This implies that eIF5B can regulate different sets of genes under different stress-inducing conditions, strongly indicating that apoptosis induction may not provide the same data set of affected genes as hypoxic induction did.

2 Materials and Methods

I created libraries of U343 glioblastoma multiforme cells under four distinct conditions: control siRNA, siRNA targeting eIF5B, control siRNA + TRAIL treatment, and siRNA targeting eIF5B + TRAIL treatment. A portion of these samples were prepared into ribosome footprinting libraries, and the remained was set aside for RNA-seq. These same treatment conditions were used for metabolomics library preparation so that they could be directly compared.

1.1 Cell Culture Reagents

1.1.1 Media, Composition, Incubation Conditions

U343 was grown in Dulbecco's Modified Eagle Medium (DMEM; Hyclone) with 4500 mg/L glucose, 4 mM L-glutamine, 1% penicillin-streptomycin (Gibco), 1 mM sodium pyruvate, and 10 % fetal bovine serum (FBS, Gibco). Cells were incubated at in a humidified incubator at 37 °C with controlled 5% CO_2.

1.1.2 Reverse transfection conditions

U343 was seeded at 200,000 cells/well and reverse transfected in 6-well plates. Transfection of siRNAs for knockdown was carried out using Lipofectamine RNAiMax (Invitrogen 13778-150) according to the manufacturers protocol for reverse transfection. Non-specific control siRNA (siC) was obtained Qiagen (1027310) and siRNA targeting eIF5B (si5B) was obtained as three individual stealth siRNAs from Invitrogen and pooled (HSS114469/70/71). Each siRNA was added at a final concentration of 20 nM in the well. Human recombinant TRAIL was obtained from Sigma (616374).

1.2 Cell Culture and Lysis Conditions

1.2.1 Cell Culture for Western Blotting

U343 cells were seeded at 200,000 cells/well and reverse transfected in 6-well plates. After 72 hours (Ribosome Profiling) or 96 hours (Metabolomics), the media was removed, the wells were washed twice with phosphate buffered saline (PBS), and the cells were removed with RIPA lysis buffer supplemented with protease inhibitors. Cells were lysed on ice in RIPA with vortexing. The samples were then spun at 10,000 rpm for 10 minutes at 4 °C and the supernatant was collected and stored at -20 °C for Western Blot analysis.

1.2.2 Cell Culture for Ribosome Profiling

U343 cells were seeded at 200,000 cells/well and reverse transfected in 6-well. plates. After 68 hours, TRAIL was added to select samples at 100 ng/mL and allowed to incubate at 37°C for four hours. After 72 hours total growth time, cells were incubated for

5 minutes at 37 °C in the presence of 100 µg/mL cycloheximide (CHX; Sigma C7698). Media was then removed from each well and they were rinsed twice and then scraped with ice-cold PBS containing 100 µg/mL CHX. Two plates for each treatment condition were pooled into a single 15 mL tube for centrifugation and lysis. Cells were centrifuged at 3000 rpm for 2 minutes at 4 °C in a 15 mL tube (Sarstedt). The pellet was then resuspended in Basic solution (0.3 M NaCl, 15 mM $MgCl_2$•$6H_2O$, 15 mM Tris, pH 7.4) and transferred to a 1.5 mL tube lysis was performed with final concentrations of 0.2 mM DTT (Sigma 43816), 100 ng/mL CHX, 12 Units Turbo DNase (Invitrogen AM2238), 0.5 % Sodium Deoxycholate (Sigma D6750), and 1 % Triton X-100 (Bio Basic;TB0198). Samples were then incubated on ice for 20 minutes with frequent vortexing to facilitate lysis. The lysis mixture was then triturated for 1 minute through a 21 G needle before incubation for a further 20 minutes on ice. Following this, the samples were triturated 10 times through a 26 G needle before centrifugation at max speed for 5 minutes at 4 °C. Cleared supernatant was transferred to a clean lo-stick RNAse free Tube (Eppendorf) and the RNA concentration was determined using Thermo Scientific NanoDrop.

1.3 Cell Culture for Metabolomics

U343 cells were seeded at 200,000 cells/well and reverse transfected in 6-well plates. After 92 hours, TRAIL was added to select samples at 200 ng/mL and allowed to incubate at 37 °C for four hours. After 96 hours total growth time, the DMEM was removed from each well and they were subsequently rinsed with 1mL 37°C warm PBS, ensuring that total rinse time was less than five seconds. Following this, liquid N_2 was poured directly onto each well to facilitate snap freezing. After liquid N_2 evaporated,

plates were placed on dry ice and moved into the fume hood. Cells were scraped in -80 °C chilled 9:1 v/v Methanol/Chloroform and subsequently centrifuged at 16,000 g for 10 minutes at 4 °C and supernatant was transferred to clean 5mL tube. Samples were then stored at -80 °C overnight and then evaporated in a passive N_2 gas chamber for 6 days.

1.4 Western Blotting Protocol

Samples were quantified with Bradford reagent and equal amounts were ran on an SDS-PAGE gel. Gels were transferred onto nitrocellulose and were subsequently blocked and treated with primary antibodies. Primary antibodies for Cas7 (Cell Signalling Tech 9492S), β-Actin (Biorad 12004163), and eIF5B (Protein Tech 13527-1-AP) were left on the blots overnight. Secondary goat anti-rabbit secondary antibody (Abcam ab97051) was treated on the blots for 1 hour at room temperature. Blots were rinsed, developed using ECL western blotting substrate (Thermo) and imaged on Amersham Imager 600.

1.5 Polysome Profiling

Cell culture used for polysome profiling was grown, harvested, and lysed in the same fashion as the samples for ribosome profiling. Samples were digested using RNAse I (Invitrogen AM2294) at 40 °C for times ranging from 0 – 60 minutes to optimize digestion. Enzymatic activity was halted with SUPERase*In (Invitrogen AM2696). Samples were centrifuged for 40 minutes at 140,000 rpm in a 10 – 50 % sucrose gradient using a Sorval 140AT rotor in a Beckman SW41 centrifuge. Fractionation and data collection was performed using Brandel density gradient fractionation system.

1.6 Ribosome Profiling

Protocol was adapted from Ingolia *et* al. 2017. Oligonucleotides were purchased from IDT, resuspended in RNAse-free H_2O and stored as aliquots in -80 °C. All experiments were performed with under rigorous RNase-Free conditions and frequent glove changes.

Pre-adenylation of each linker used was done prior to starting the experiment. This was performed by incubating each linker with Mth RNA ligase (NEB E2610S) for one hour at 65 °C followed by a five minute incubation at 85 °C to deactivate the enzyme. Adenylated linkers were then purified using Oligo Clean & Concentrator kit (Zymo D4060).

1.6.1 RNA Size Selection

Replicates were performed one set at a time and the amount of RNA used for library preparation was determined based on RNA yield. The exact amount of RNA per replicates is included in the relevant section and was between 15-60 µg total RNA per sample. For a given replicate, an equal amount of RNA was taken from each sample and digested with RNAse I for 50 minutes at 40 °C after which samples were quenched with SUPERAse*In. Samples were loaded on top of a 1 M sucrose cushion and centrifuged in an S140-AT (Thermo) fixed angle rotor for 40 minutes at 140,000 rpm. Supernatant was removed and RNA purification was performed by dissolving the pellet in Trizol (Invitrogen 15596026) and processing the samples using Directzol RNA Miniprep Kit (Zymo R2050). Samples were then isopropanol precipitated overnight at -20 °C and resuspended in 10 mM Tris pH 8.

Size selection was performed by running each sample for 65 minutes at 200 V in a 15 % Urea-TBE gel, staining the gel with SYBR Gold (Invitrogen S11494) and excising fragments 17 – 34 nt in size. Visualization was performed using UV and references images were obtained using Amersham Imager 600. Excised gel fragments underwent RNA extraction overnight followed by an overnight isopropanol precipitation at -20 °C and resuspended in 10 mM Tris pH 8.

1.6.2 Dephosphorylation, Linker Ligation, Pooling, and Reverse Transcription

Size-selected samples were incubated for one hour at 37 °C with T4 PNK (NEB M0201S) in order to dephosphorylate the 3' end of the RNA fragment. Following this, custom pre-adenylated linkers were ligated to the 3' end of each RNA fragment by T4 Rnl2(tr) (NEB M0242L) for three hours at 22°C. Each pre-adenylated linker contains a Unique identifier sequence to distinguish each sample. As a result, each sample from a given set were pooled and concentrated using Oligo Clean & Concentrator kit.

Reverse transcription was performed using a custom primer complimentary to the ligated linker. This was performed using Superscript III (Invitrogen 18080-044) as the reverse transcriptase at 55 °C for 30 minutes, followed by 20 minutes at 70 °C in the presence of NaOH to hydrolyze the RNAs. Reverse transcription products were resolved on a 10 % Urea-TBE gel at 200 V for 70 minutes. Gel was stained with SYBR Gold, visualized with UV, and reference images were taken with the Amersham Imager. Fragments of the correct size were excised and extracted in a DNA extraction buffer overnight, followed by an overnight isopropanol precipitation at -20 °C. Samples were resuspended in 10 mM Tris pH 8.

1.6.3 Circularization and ribosomal RNA Depletion

Circularization of the RT size-selection product was performed using CircLigase (Lucigen CL4111K) with two rounds of 60-minute incubations at 60 °C followed by a 10 minute incubation at 80 °C to inactivate the enzyme. Ribosomal rRNA reduction was performed using a pool of biotinylated oligonucleotides complimentary to human rRNA sequences. The samples to be depleted were hybridized with the oligonucleotide mix were denatured for two minutes at 95 °C. MyOne Streptavidin C1 Dynabeads (Invitrogen 65001) were incubated with the hybridization mix for 20 minutes at room temperature at 400 rpm in a thermomixer. A magnet was then used to remove the Dynabeads allowing the supernatant to be collected where it was subsequently precipitated in the presence of Isoproponaol overnight at -20 °C. The precipitated pellet was resuspended in 10 mM Tris pH 8.

1.6.4 qPCR, PCR, and Quality Control

qPCR was performed using Perfecta SYBR Green Master Mix (Quantabio) with the following conditions: 15 minutes at 95 °C, followed by 40 cycles of: 10 seconds at 94 °C, 20 seconds at 54 °C, and 30 seconds at 72 °C. A serial-diluted standard curve of a control oligonucleotide is used to determine the concentration of the circ DNA sample. This concentration is used to determine the optimal number of library-construction PCR cycles to perform as shown in Ingolia *et al*. 2017.

PCR is performed using Phusion polymerase (NEB M0530S), custom forward primer, and UMI containing reverse primer. Depending on the concentration of the qPCR

sample, approximately 10-11 PCR cycles are performed. The amount of PCR cycles performed was optimized for each individual sample (the number of specific samples are included in the relevant sections). The PCR amplification conditions are as follows: 30 seconds at 98 °C, followed by 10-11 cycles of: 10 seconds at 98 °C, 10 seconds at 65 °C, and 5 seconds at 72 °C followed by a final elongation of 5 minutes at 72 °C. PCR product is cleaned and concentrated in DNA Clean & Concentrator kit (Zymo D4003).

Purified PCR product was resolved in an 8 % Native-TBE gel for 55 minutes at 180 V. The gel was visualised, excised, and extracted as previously described for DNA extraction. DNA was precipitated as previously described and resuspended in 10 mM Tris pH 8. DNA was analyzed for purity with Agilent Bioanalyzer on a High sensitivity DNA chip (Agilent 5067-4626).

1.6.5 RNA Purification for RNA-seq

RNA was isolated and purified from the original lysate used for each sample for which a ribosome-protected footprint library was prepared. 100 µL of lysate was mixed with 300 µL of Trizol and processed with Directzol RNA miniprep kit. RNA was stored at -80 °C until it was sent off for RNA-seq library preparation.

1.7 Metabolomics NMR sample Prep

The pellet was resuspended in 560 µL of pH 7.4 potassium phosphate buffer and 140 µL of D_2O containing 0.02709% w/v trimethylsilylpropranoic acid (TSP) as a chemical shift reference for ^1H NMR spectroscopy. Potassium phosphate buffer was created using a 4:1 ratio of dibasic (K_2HPO_4) to monobasic (KH_2PO_4) potassium phosphate with a

concentration of 0.625 M. 3.75 mM sodium azide (NaN_3) was added as an antimicrobial agent. Samples were vortexed until fully dissolved, then centrifuged at 16,000 g at 4 °C for 20 minutes. 550 µL aliquots of each sample were transferred to a 5 mm NMR tube for data acquisition. NMR spectra was acquired using a 700 MHz Bruker Avance III HD spectrometer. One-dimensional and three-dimensional shimming were performed before data acquisition to increase the signal to noise ratio by correcting any inhomogeneities in the applied magnetic field. Data were acquired utilizing a 1-D NOESY gradient water suppression pulse sequence, 1024 scans, obtaining 128k data points, zero filled to 256k, with line broadening to 0.3 Hz, and automatic phase and baseline correction.

1.8 Metabolomics Statistics and Analysis

MATLAB was utilized to perform the following procedures (MathWorks, MA, USA). The spectra underwent a data reduction step utilizing dynamic adaptive binning followed by manual correction.[53] The data sets were pareto scaled and normalized using recursive segment-wise peak alignment.[54,55] Wilcoxon Mann-Whitney U (MW) was utilized to identify significant alterations in metabolite concentrations between comparison groups, operating on the binned spectra.[56] Metabolites were identified using Chenomx (Chenomx Inc., Edmonton, Alberta, Canada), and cross referenced with the Human Metabolome Database (HMDB).[57] Metaboanalyst was utilized to perform pathway topology analysis, using the identified metabolites, the Kyoto Encyclopedia of Genes and Genomes (KEGG), Small Molecule Pathway Database (SMPDB), and HMDB libraries.[57-59] A custom R script was used for data visualization including Principal Component Analysis (PCA), an unsupervised statistical test employing the first two principal

components that contribute to the greatest variation in the data, and heat maps, an unsupervised hierarchical data clustering technique that display the magnitude of variation in metabolite concentrations.[60]

3 Results

3.1 Metabolomics

3.1.1 Protocol Development

Protocol adapted from Kostidis *et al* for use with U343 and with Montina lab's NMR pipeline.[61] In their mammalian metabolomic tutorial, Kostidis *et al* present a case study example for BHP2-7 cell line – a papillary thyroid carcinoma (PTC). While their protocol was not the specific tissue or cancer type that I was growing, it was a representative mammalian solid tumour cell culture. This was very important due to the fact that all experience the Montina lab had up to this point was with either biofluids or solid tissues, so I had to determine exactly how to go about growing, harvesting, and testing exactly how much cell mass I required.

In their protocol, Kostidis *et al* grew their cell culture in 10 cm dishes with the aim of achieving 80-90% confluency after 72 h in culture to prevent metabolomic changes associated with overcrowding or media depletion. Notable changes from their protocol include growing my cell culture in 6-well plates and optimizing the seeding densities for efficient RNAi treatment. Fortunately, due to the extremely well-written tutorial, very little adjustments from their sample protocol were required to collect samples for metabolomic analysis.

3.1.2 Optimization

To my knowledge neither our lab nor the Montina lab had performed any cell culture NMR, so this was new for both of our labs. Therefore, by using Kostidis *et al*'s protocol in combination with the existing pipeline in the Montina NMR lab, we derived a strategy to first perform a series of test experiments prior to the actual gathering of samples for NMR analysis. Cells were grown, lysed, and prepared as described in materials and methods. Simultaneously to those plates, a single well of a 6-well plate for each condition was grown and harvested for western blot confirmation of eIF5B knockdown and TRAIL efficiency. The knockdown and TRAIL efficiency western blots can be seen in Figure 1. β-actin is used as a loading control, and Cleaved Cas-7 is used as a measure of TRAIL activity – a marker previously shown to be an accurate measure of adequate eIF5B depletion and TRAIL activity.[15]

Two initial experiments were performed before a set of 6 replicates was collected. The first was the generation of two samples, both treatment condition eIF5B-KD and TRAIL treatment: one grown from a single 6-well plate, and one grown from two 6-well plates. This was performed with that specific treatment condition since it is expected to have the least cell mass due to early apoptosis. This experiment performed determined the optimal number of reads for maximum resolution to be 1024 reads, as well as demonstrating that one plate provided sufficient cell mass to yield adequate metabolite resolution. The second experiment consisted of one sample of each treatment condition to assess whether the lysis conditions used provided sufficient lipid removal for each treatment condition. All 4 samples showed a good enough baseline, providing me with the information I needed to generate 6 more replicates.

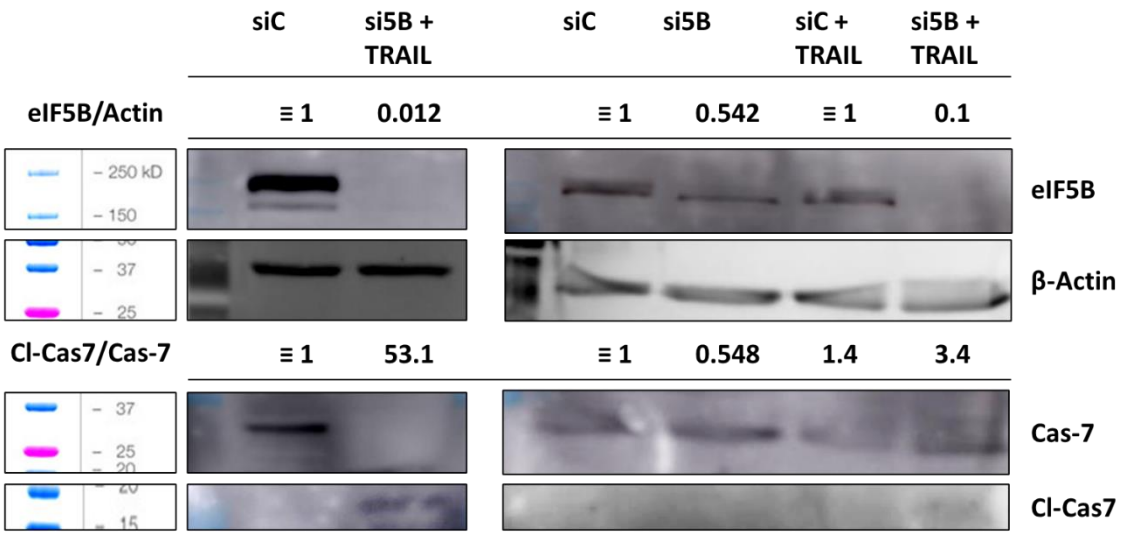

Figure 1. Depletion of eIF5B and TRAIL activity. Western Blots of eIF5B and Cas-7 demonstrating eIF5B KD and TRAIL activity for test experiment 1 (left), and test experiment 2 (right). Caspase 7 is visible as a band at approximately 35 kDa, with its cleaved form appearing as a band around 17 kDa. Cl-Cas7 bands are visible under conditions of si5B and TRAIL treatment in both left and right panels.

All 6 replicates showed adequate eIF5B knockdown and TRAIL activity (Figure 2). As a result, all 6 replicates can be trusted, or at the very least, the frozen samples can be trusted and can be rerun if need be. Additionally, each replicate also had samples of the media at the time of harvest collected. These samples did not have NMR performed on them; however, they could at any future time as they store very well at -80 °C and were labelled and stored accordingly.

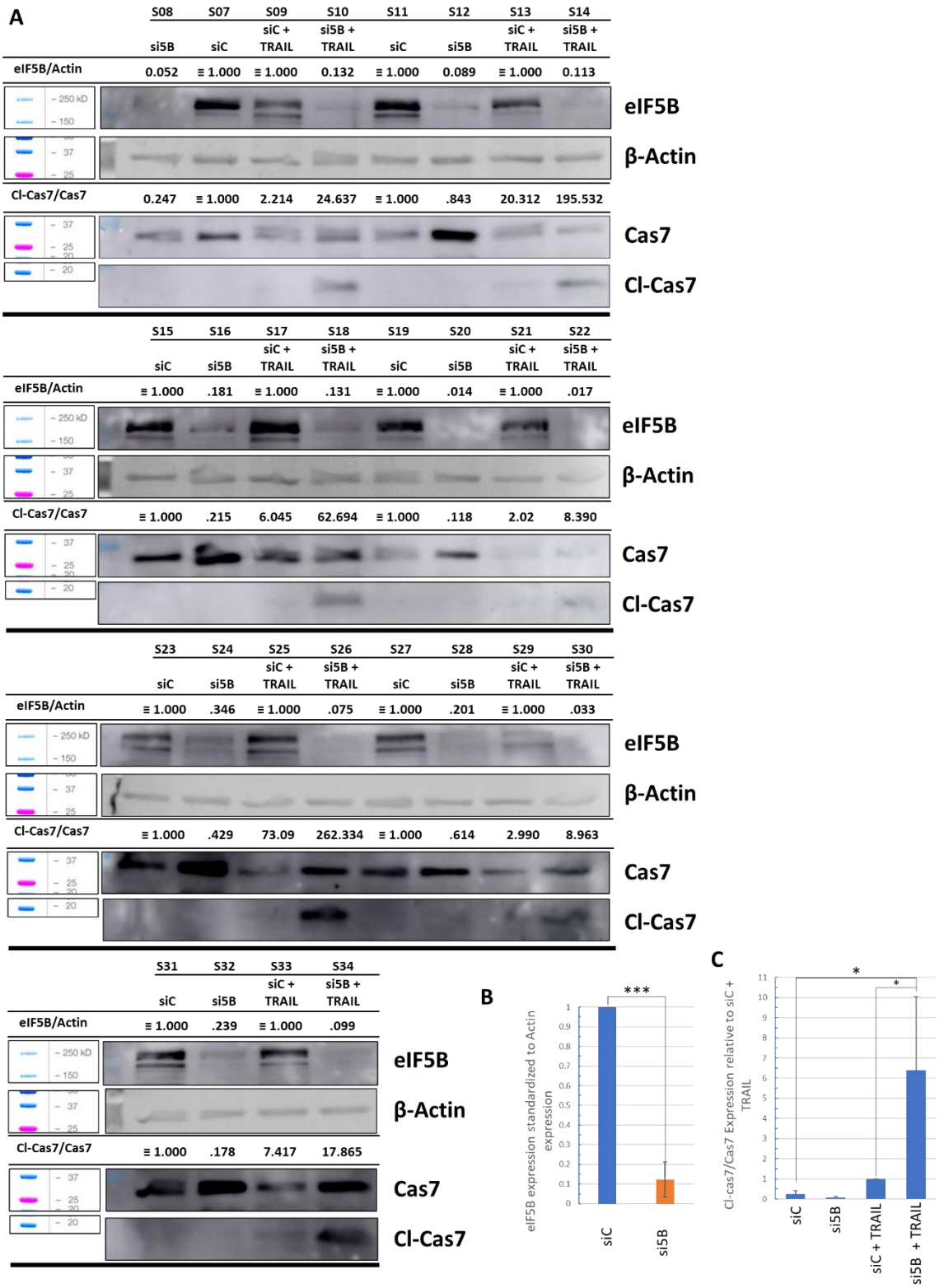

Figure 2. Knockdown of eIF5B and TRAIL activity for Metabolomics Replicates 1-6. An average of eIF5B knockdown and TRAIL activity shown via cleavage of Cas7 across all 7 replicates (Panels B,C) showing significant decreases in eIF5B under si5B conditions

(Panel B) and significant Cas7 cleavage under si5B + TRAIL treatment (Panel C) as determined by students T test. Western Blots of eIF5B and Cas-7 demonstrating eIF5B KD and TRAIL activity for replicates 1-7. **a)** Replicates 1 & 2. **b)** Replicates 3 & 4. **c)** Replicates 5 & 6. **d)** Replicate 7 was harvested using 8.1:0.9:1 MeOH/$CHCl_3$/dH_2O. Caspase 7 is visible as a band at approximately 35 kDa, with its cleaved form appearing as a band around 17 kDa. Cl-Cas7 bands are visible under conditions of si5B and TRAIL treatment in each panel.

3.1.3 Metabolomics Results

All variables as well as bins found to be significant by Mann-Whitney (MW) testing were utilized for data visualization. There was a total of 256 bins, 100 were found to be significant for the si5B/si5B + TRAIL comparison; 73 for siC/si5B; 103 for siC/siC + TRAIL; and 88 for siC + TRAIL/si5B + TRAIL. PCA's generated using all variables display a high degrees of data separation for all comparison groups as seen in Figure 3. si5B/si5B + TRAIL, siC/si5B + TRAIL, and siC/siC + TRAIL comparisons display overlap of the 95% confidence interval (CI), denoted by the shaded ellipses. Complete separation is observed in the siC/si5B + TRAIL comparison. No misclassifications are observed in the PCA of siC/siC + TRAIL (Figure 3b), whereas three misclassifications are seen in both the siC + TRAIL/si5B + TRAIL and si5B/si5B + TRAIL comparisons PCA's (Figures 3c,d). Heatmaps were generated utilizing the bins identified as significant by MW. There were no misclassifications in any comparison's heatmap, and clear clustering of metabolite concentrations is shown (Figure 3). The unsupervised separation seen here supplements the PCA's findings.

Pathway topology analysis was completed separately for each comparison, using the bins found to be significant by MW, and depict the potential metabolic pathway impact due to differences in metabolite concentrations.

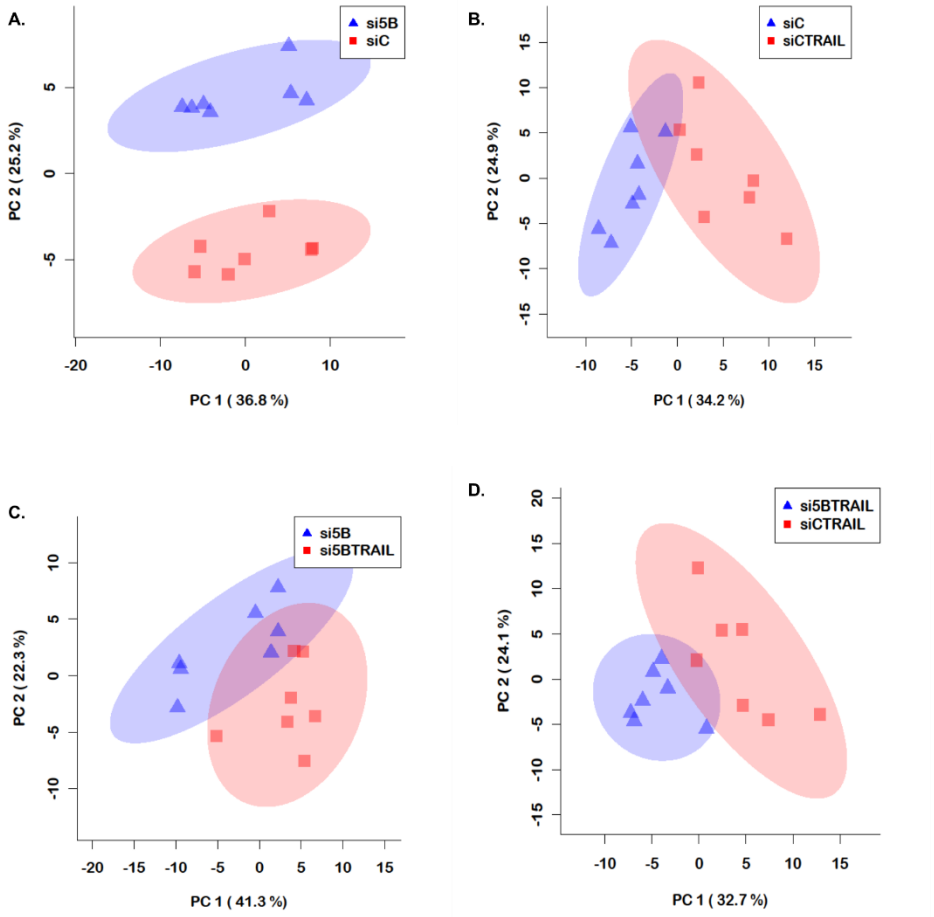

Figure 3. Principal Components Analysis (PCA) scores plots. a) siC/si5B. b) siC/siC + TRAIL. c) si5B/si5B + TRAIL. d) siC + TRAIL/si5B + TRAIL. Figures were generated using all 256 variables. The shaded ellipses indicate the 95% confidence interval (CI). The x and y-axis plot the variance explained by the first and second principal components respectively.

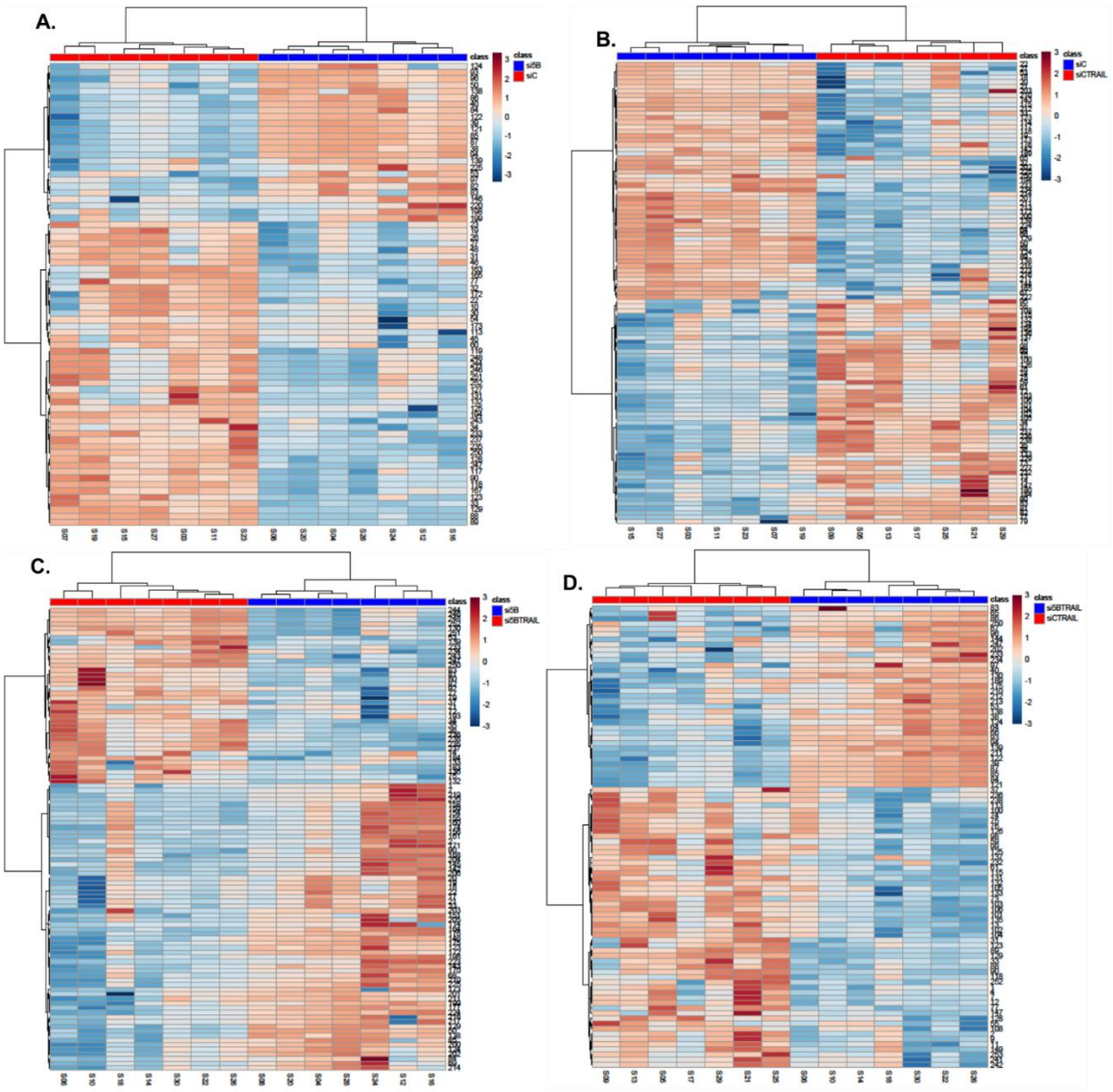

Figure 4. Heat maps depicting unsupervised classification and hierarchical clustering of metabolic profiles. a) siC/si5B. b) siC/siC + TRAIL. c) si5B/si5B + TRAIL. d) siC + TRAIL/si5B + TRAIL. The heat maps illustrate up-regulation (red) versus down-regulation (blue) of metabolites identified as significant by Wilcoxon Mann-Whitney U testing: 100 for si5B/si5B + TRAIL; 73 for siC/si5B; 103 for siC/siC + TRAIL; and 88 for the siC + TRAIL/si5B + TRAIL comparison.

Figure 5 shows a list of the metabolomic pathways differentially regulated in each set of comparisons. Each list of pathways is ranked according to the -log(p) value for each pathway between two distinct comparative groups – that is, siC/si5B (5a), siC/siC +

TRAIL (5b), si5B/si5B + TRAIL (5c), and siC + TRAIL/si5B + TRAIL (5d). However, while these comparisons are quite useful for generating an overview and initially looking into differences under treatment conditions I do not go into a great amount of detail regarding these pathways. Part of the reason for this is that the greatest significance (not necessarily greatest impact) that is ranked #1 for each set of comparisons is the aminoacyl-tRNA biosynthesis pathway. What this means is that each group differed significantly from each of its comparisons in this pathway, which while initially appearing interesting, specifically means that any change I make affects this pathway. Ultimately, I want to investigate the impact that depleting the cells of eIF5B has on metabolite expression, and more specifically, how si5B + TRAIL differs significantly from siC + TRAIL. Notably then, Figure 5d which compares pathway differences in those two conditions should be of the upmost interest. However, when looking more closely at the most significant pathways (farther along the x-axis to the right in Figure 5), I discover that the majority of the pathways which are different between siC + TRAIL and si5B + TRAIL do not seems to be an si5B + TRAIL specific trend, but rather as a result of either eIF5B depletion or TRAIL depletion on their own. Hence, as can be seen in Figures 6-8, I decided to look more closely at individual metabolites so that I could explore the specific differences in metabolites which are up or down specifically under only 1 or 2 of my treatment groups.

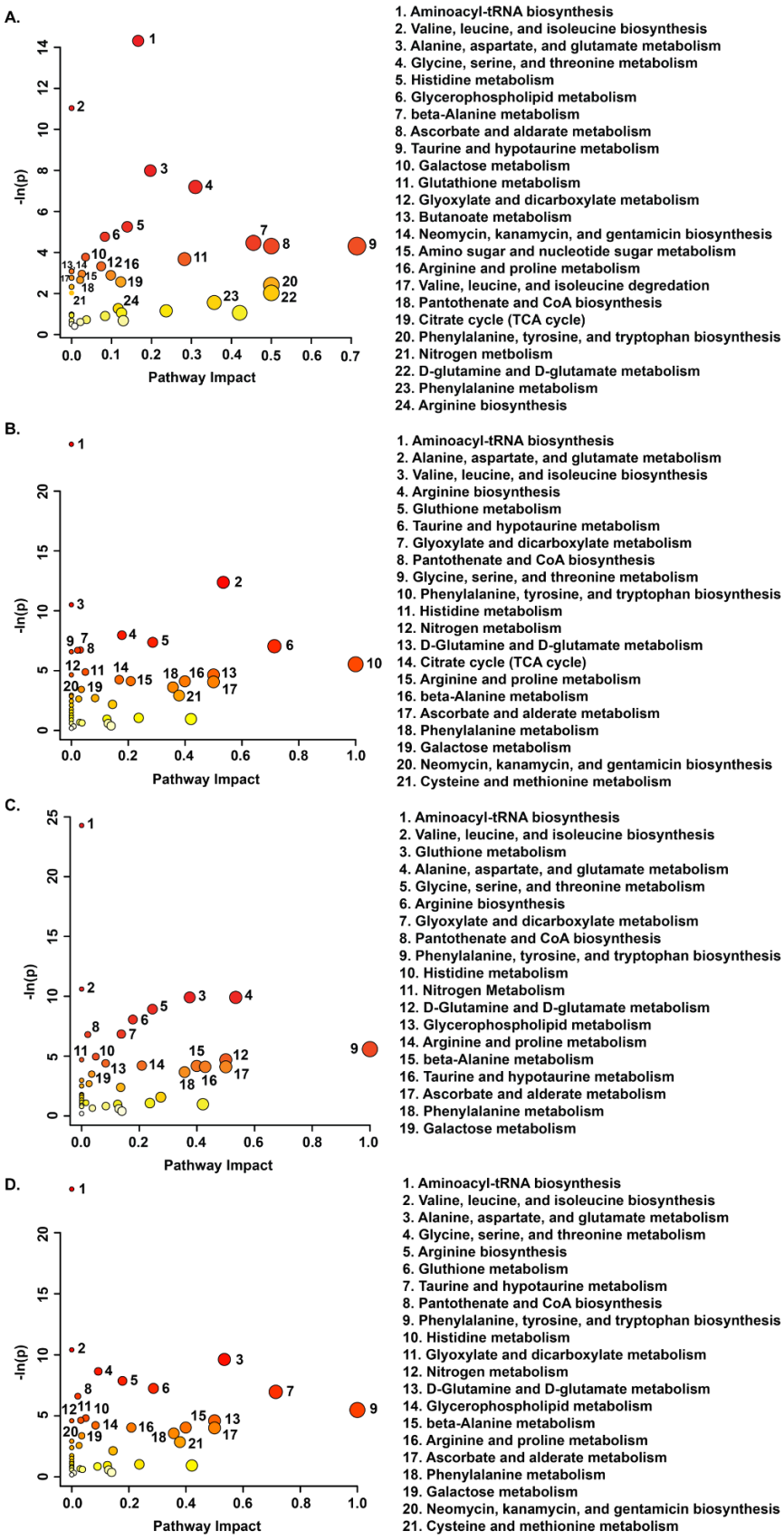

Figure 5. Metabolic pathways altered. a) siC-si5B. b) siC/siC + TRAIL. c) si5B/si5B +

TRAIL. d) siC + TRAIL/si5B + TRAIL. The x-axis displays the potential impact of the significantly altered metabolites on the pathway. The y-axis shows the negative natural log of the p-value for each pathway with an increasing value corresponding to a smaller p-value (-ln(0.05) = 3.0). Pathway topology analysis were carried out using the metabolites that were identified as significant by Wilcoxon Mann-Whitney U testing.

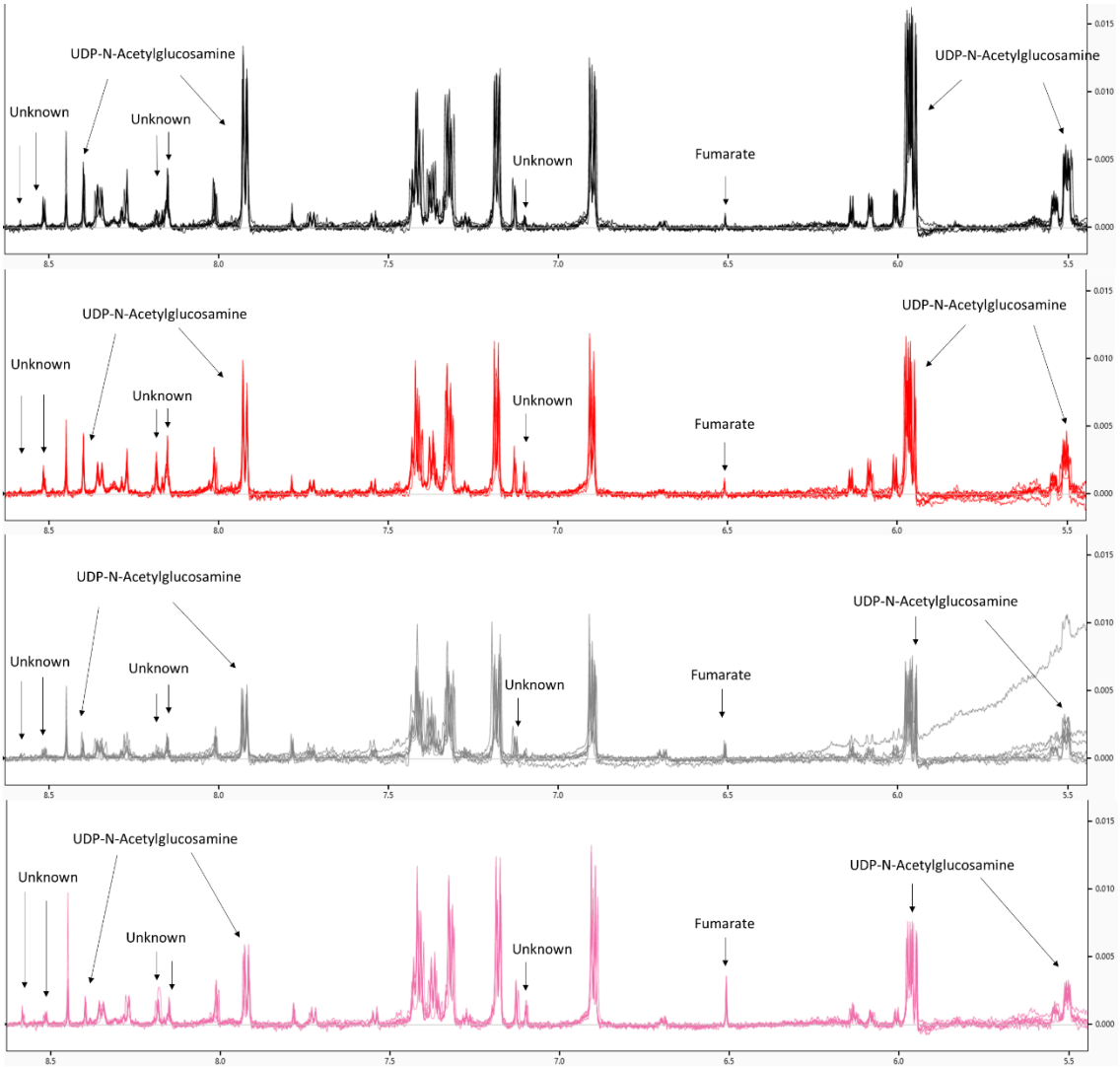

Figure 6. 1H NMR Spectra from ppm 5.5-8.75. Peak height directly proportional to relative concentration of each metabolite(s) as n=7. Each panel displays all 7 replicates for each of siC (black), si5B (red), siC + TRAIL (grey), and si5B + TRAIL (pink).

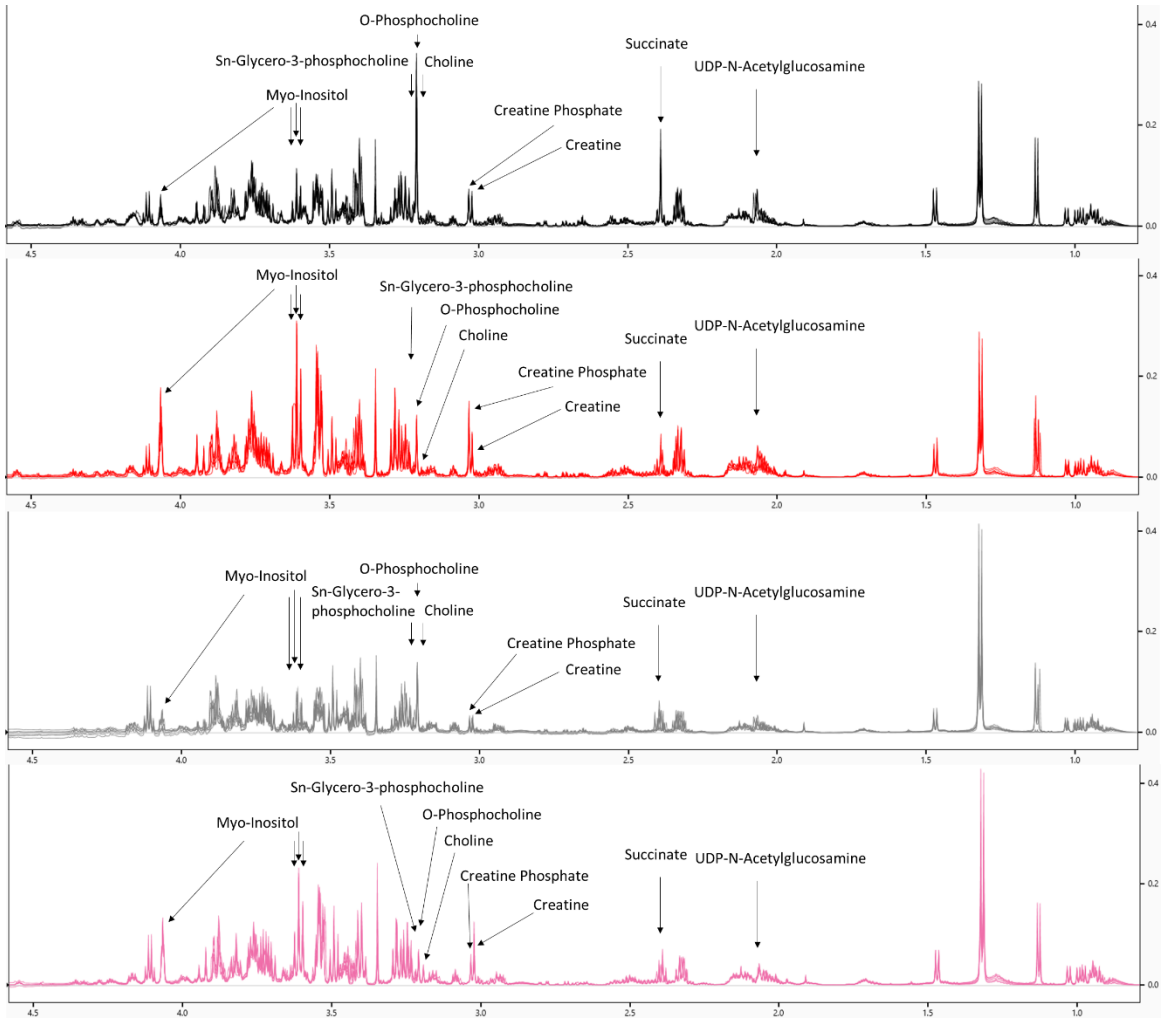

Figure 7. 1H NMR Spectra from ppm 1.0-4.5. Peak height directly proportional to relative concentration of each metabolite(s) as n=7. Each panel displays all 7 replicates for each of siC (black), si5B (red), siC + TRAIL (grey), and si5B + TRAIL (pink).

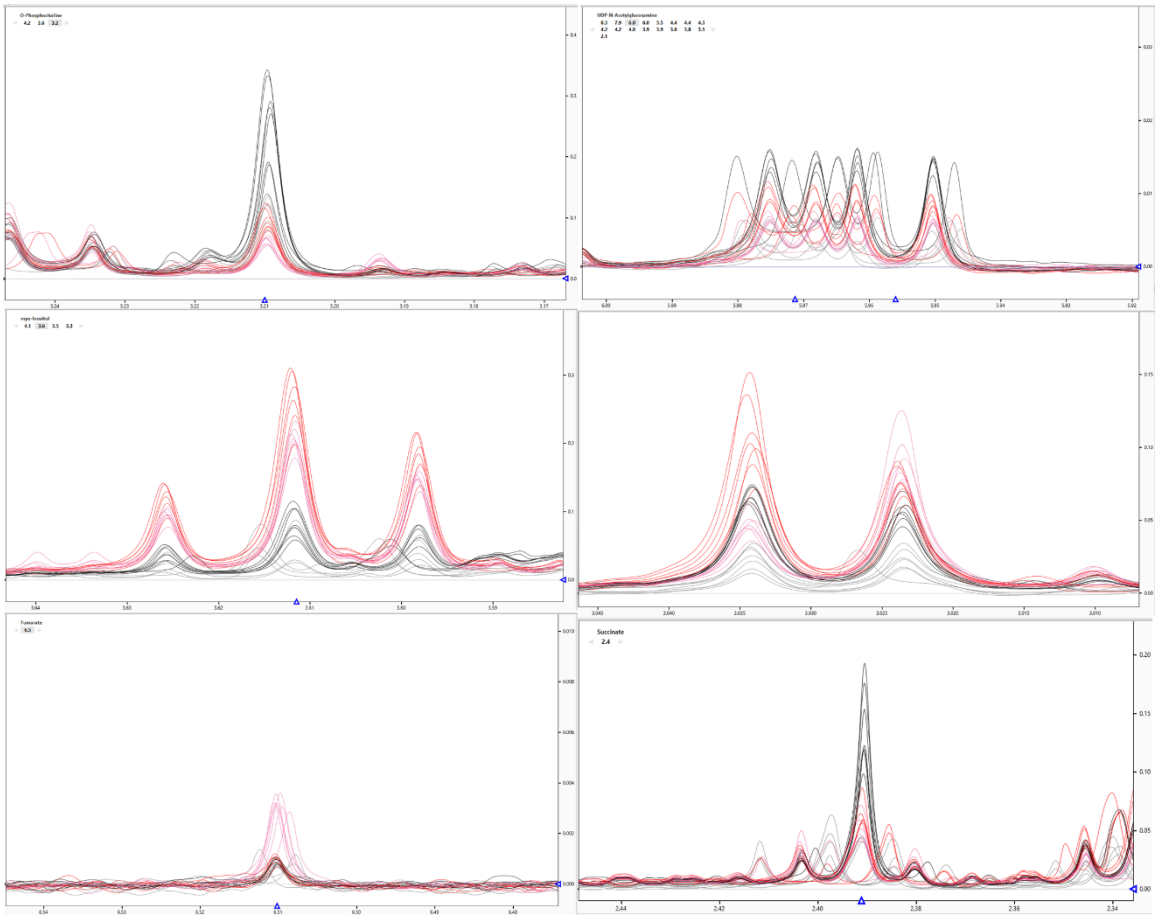

Figure 8. 1H NMR Spectra of specific metabolite peaks. Peak height directly proportional to relative concentration of each metabolite(s) as n=7. Each panel displays all 7 replicates for each of siC (black), si5B (red), siC + TRAIL (grey), and si5B + TRAIL. Only one representative set of peaks are shown for each metabolite based on a low concentration of overlapping metabolite spectra. Top left: Sn-glycero-3-phosphocholine @ 3.22 ppm, O-phosphocholine @ 3.21 ppm, and Choline @ 3.195 ppm. Top right: UDP-N-Acetylglucosamine. Center left: Myo-inositol. Center right: left peak is creatine phosphate, right peak is creatine. Bottom left: Fumarate. Bottom right: Succinate @ 2.39 ppm.

When comparing individual metabolite levels with the spectra data shown in Figures 6 and 7, a few metabolites stand out as being expressed/present at different levels under my treatment groups. Notably, while I tried to label each peak in Figures 6 and 7 which were differentially regulated to a significant extent, there are a few which are labelled with unknown – these peaks could not be identified and/or did not appear within the Mann-Whitney significant bins and so were not initially considered. Six primary metabolites were

selected and displayed in Figure 8 based on their consistency, degree of differential metabolite levels, and importance. To generate the images for Figure 8, a single peak or set of peaks was selected for each metabolite of interest based on its clarity, ease of imaging, and least degree of overlapping metabolites. Further, each peak is representative of the group of peaks associated with the metabolite and not outliers from the overall metabolic trend. These metabolites are choline, UDP-N-acetylglucosamine, inositol, creatine, fumarate, and succinate.

As can be seen in Figure 8, total choline is shown as 3 distinct peaks: Sn-glycero-3-phosphocholine, O-phosphocholine, and choline which display peaks at 3.22, 3.21, and 3.195 ppm respectively. In this figure, we see levels of glycerophosphocholine decreasing slightly under siC + TRAIL treatment, with larger decreases under si5B and si5B + TRAIL sample groups. Phosphocholine levels decrease under both TRAIL and si5B treatment alone, as well as decreasing further under both si5B + TRAIL treatment. Quite interestingly, levels of choline decrease only slightly under either TRAIL or si5B treatment alone, but then increase under si5B + TRAIL treatment. UDP-N-glucosamine levels decreased under both TRAIL and si5B treatment on their own, but combined treatment was not significantly lower than TRAIL treatment on its own. Myo-inositol was dramatically higher when eIF5B was knocked down either on its own or in combination with TRAIL. TRAIL did not have a significant impact on myo-inositol levels on its own but did result in a minor decrease in the si5B + TRAIL sample. Creatine and phosphocreatine, as shown in Figure 8 center right panel, show quite an interesting trend. Both creatine and phosphocreatine decrease significantly under TRAIL treatment and increase under eIF5B treatment – however, under both si5B and TRAIL treatment in combination, I see levels of creatine increasing at the same time as levels of phosphocreatine decrease. This suggests

that there is an interaction occurring when the cells are treated with TRAIL while eIF5B is depleted which does not occur under conditions of si5B or TRAIL treatment on their own. Lastly, the bottom two panels of Figure 8 show the single peak for both fumarate (left) and succinate (right). Levels of fumarate remain largely unchanged under both si5B and TRAIL treatment on their own, but under combination treatment levels rise almost 3.5x. The peak for succinate is shown on the right due to the fact that succinate is directly upstream of fumarate in the citric acid cycle, as well as to demonstrate that levels of succinate decrease dramatically under either si5B or TRAIL treatment on their own, and do not appear to decrease further under combined treatment. Between these different metabolites it is clear that eIF5B and TRAIL both show distinct metabolic trends that, when combined as treatment, show trends opposite of what either on their own had on metabolite expression.

3.2 Translatome Profiling

3.2.1 Optimization

3.2.1.1 RNase Treatment Optimization

On the recommendation of our collaborators, I performed an RNase I digestion optimization on the GBM cell-line U343. The goal of the RNase I digestion on the RNA lysate is to break down polysomes into monosomes without degrading the ribosomes themselves. If performed properly, this results in the majority of the sample existing as ribosome-protected footprints – the 28-32 nt region of RNA protected by the ribosome – reducing the whole sample in to 28-32 nt fragments. Ingolia *et al* recommends RNase digestion for 45 minutes at RT; however, our collaborators previously found the treatment conditions of 50 minutes at 40 °C ideal for a separate GBM cell line.[50] Additionally, in

contrast with the Ingolia *et al* protocol, it was strongly recommended by my collaborators to optimize the RNase digestion for each new cell line used as the optimal digestion time and temperature can vary with lab, tissue type, and cell line.[50]

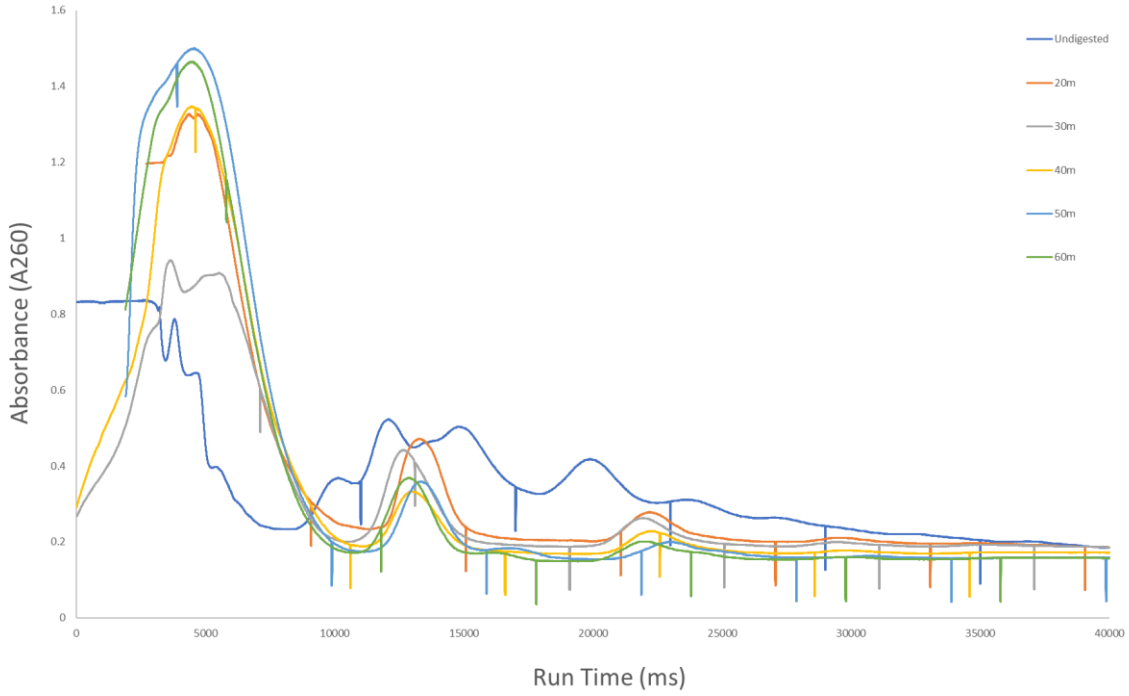

Figure 9. RNase I digestion optimization. U343 was digested using 1 uL Ambion RNase I for every 50 ug of RNA, as determined by Nanodrop. Digestion was performed for 0, 20, 30, 40, 50, and 60 minutes at 40 °C before being quenched with Ambion SUPERase*In and placed on ice. Longer incubation times reflect decreases in polysomes and increase in monosome peak height up to 50 minutes.

Through the optimization of RNase I digestion in U343, it was determined that digestion for 50 minutes at 40°C was ideal. At this time point, decreases in di-somes and polysomes were witnessed, along with the greatest number of whole ribosomes present. By 60 minutes, the monosome peak had shrunk without a corresponding decrease in size amongst the polysome peaks, indicating over-digestion. For further experimentation, RNase I digestion was performed at 40°C for 50 minutes.

3.2.1.2 Lysis Optimization

One issue I experienced was trying to acquire a concentrated amount of RNA from U343 that also showed high knock-down efficiency with our siRNA treatment. Previously, we determined that a more consistently high knockdown of eIF5B was achieved growing U343 in 6-well plates rather than with 10 cm plates. Additionally, since the samples generated for metabolomics were grown in 6-well plates, doing the same here would provide the greatest amount of consistency and therefore highest degree of correlation between the samples.

I started by seeding 2 x 10^5 cells / well and reverse transfecting with the siRNAs, a number which was chosen because it worked well for production of samples for western blots in the past, and therefore had a verified knockdown after 4 days. Previously, we have also seeded 3 x 10^5 cells for 3 days, but this 4-day treatment allowed me to monitor my growth over the treatment and harvest early if need be. Cells were incubated with TRAIL for 4 hours at 37 °C, treated with cycloheximide (CHX) for 5 minutes, rinsed, and collected in lysis buffer. These conditions did not vary through optimization; however, due to poor concentration, two 6-well plates were used for each treatment condition in the final sample preparation.

Samples were harvested from 6-well plates, centrifuged, and resuspended in 425 µL of polysome buffer. This buffer does not contain either CHX, detergent, or DDT; these were added separately so that they could be optimized should that be required – which it was. Initial detergent concentrations were based on a protocol received from our collaborators, which contained 0.025% Triton X-100 and 0.025% Sodium Deoxycholate. This was far too little detergent and yielded only 6 µg of RNA per plate in the least concentrated sample. To combat this, on the next set of plates I increased the detergent

concentrations by 20x to 0.5% Triton X-100 and 0.5% Sodium Deoxycholate. To test this, so as not to waste reagents, I seeded a single well for each test conditions instead of a full plate and added a second step to be tested which was trituration of the lysis solution with a 26G needle. Through combining these two changes, the concentration of my sample was sufficient for both Ribo-seq library preparation and RNA-seq; however, when I scaled it up to a full 6-well plate, the lysis did not scale linearly and I did not have enough sample to use. The total RNA per plate was approximately 15 µg this time, which while higher than the initial lysis, was still insufficient.

At this point, I decided to investigate whether it was a blanking issue, and if there was enough RNA by running it out on an agarose gel. As seen in Figure 10a, 10 µL of my 500 µL lysate was run on an agarose gel and I was able to see distinct ribosomal subunits as indicated in Figure 10. Unfortunately, due to the increase in the lower band present in my TRAIL treated lanes, it also looked like TRAIL might be affecting the quality of my RNA. As a result, I needed to determine if this was a single aberrant event, or whether TRAIL was indirectly causing degradation of my RNA, and whether we needed to adjust for that or change treatment conditions altogether.

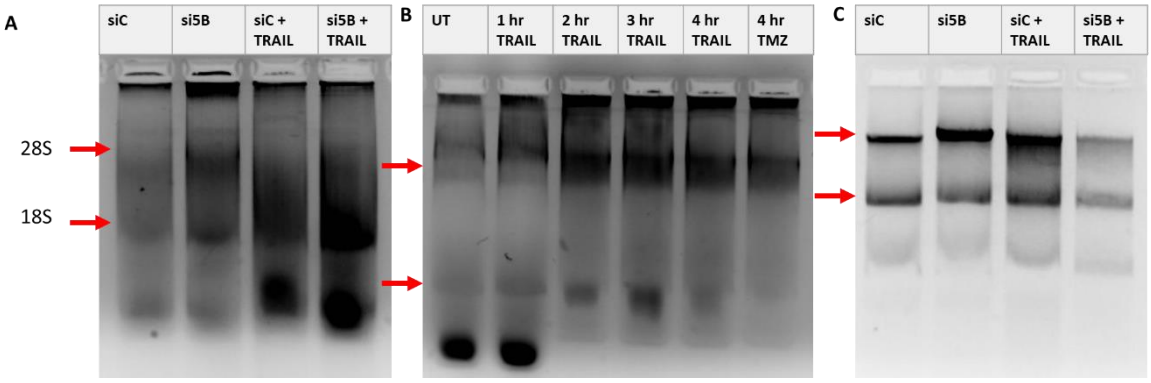

Figure 10. Agarose gels of RNA lysates. A small portion of RNA lysate was run on an EtBr stained 1% agarose gel and visualized with UV. **a)** RNA lysate immediately following lysis. **b)** Cells were treated with either TRAIL or temozolomide (TMZ) before lysis. **c)** The same sample from a), but centrifuged on a sucrose cushion and re-dissolved in polysome buffer to isolate ribosomes. Approximate locations for complete ribosome

components are indicated on each panel; smearing is visible between the 28S and 18S ribosomal subunits under TRAIL treatment in panel A.

To check whether TRAIL was degrading my RNA or not, as can be seen in Figure 10b I treated my samples with TRAIL with multiple time points from untreated (zero hours) to 4 hours (the length of treatment from first samples). Simultaneously, I treated one well with TMZ as a control. This was done because, in previous experiments, we have found eIF5B depletion to sensitize cells to TMZ-induced apoptosis in a similar fashion to TRAIL. If TRAIL had been causing issues with RNA quality, I would have proceeded with treatment of TMZ instead of TRAIL. Following this, the "degraded" samples from Figure 10a were loaded onto a sucrose cushion and centrifuged for 40 minutes at 140,000 rpm in a S140-AT rotor to pellet the ribosomes and were subsequently resuspended in 100uL of polysome buffer. Shown in Figure 10c, while there was potential ribosome degradation in the sample as shown in Figure 10a, there was still clearly intact ribosomes. As a result, I concluded that TRAIL was not the cause of the degradation I saw in Figure 10a as the result from Figure 10a was not replicated.

Following this, the next batch of samples were lysed with the following tweaks to the protocol: based on further reading information, I added an additional 1 mL rinse of cold PBS to remove the physical cells from the plate to ensure complete removal, adjusted the concentration of Triton X-100 to 1%, and increased the amount of time the samples sat on ice from 10 minutes with vortexing to 30 minutes with vortexing. These changes increased my RNA yield to approximately 40-60 µg which was more than enough to begin library generation.

3.2.1.3 Development and Optimization of RFA Library Preparation

The first complete run-through of my library preparation did not get very far, as I ran into my first error when I attempted to extract DNA from my gel following the reverse transcription step. The yellow circle in Figure 11a indicates what size I expected to see on the gel; however, while the expected band wasn't visualized, I excised the region of expected size as well as the band that was visualized and reran it on a 10% Urea-TBE gel to increase resolution. Unfortunately, Figure 11b clearly shows a lack of any elongated product of the correct size. However, while the product was not the correct size, it did happen to coincide with the size of the No insert linker only control. Hence, it indicated that one of a couple possible errors occurred: the linkers may not have been properly pre-adenylated, which would prevent ligation with the ligase used, perhaps the reaction did not de-phosphorylate, or perhaps the ligation failed due to the ligase itself.

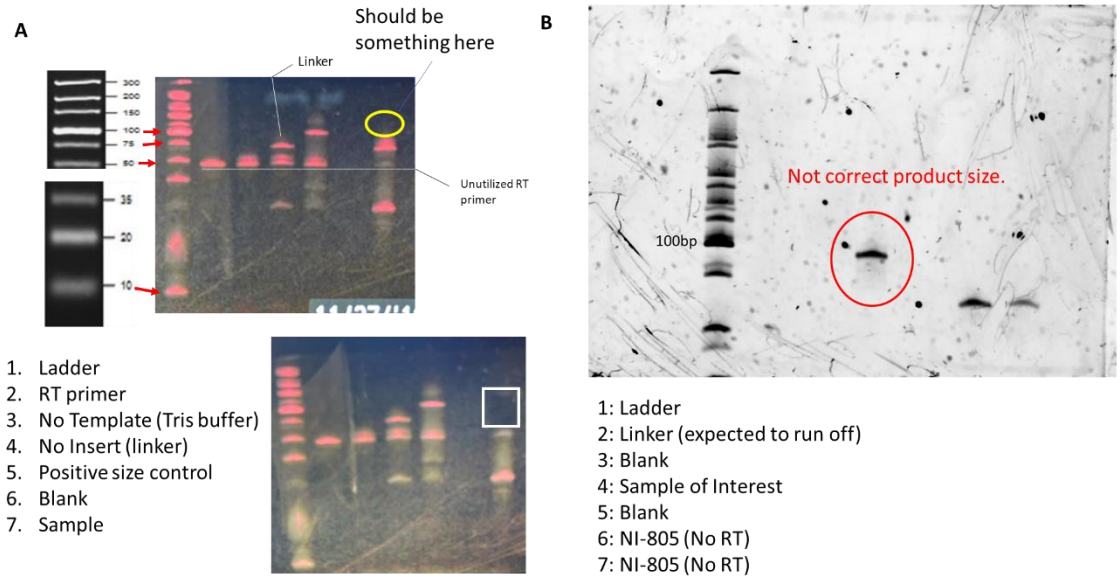

Figure 11. RFA ligation Troubleshooting. **a)** 15% Urea-TBE gel stained with SYBR gold. Lane 7 contains pooled set of all samples. **b)** 10% Urea-TBE gel stained with SYBR gold rerun of the excised sample from **a)**. The expected band of >100bp is not visible in either panel A or the expanded panel B.

Following this, I set up an experiment to investigate each possible cause for not receiving an RT band of the correct size. First, I generated a new set of lysates of U343 with no treatments of reverse transcription so as not to waste reagents. This was because I wanted to generate a large amount of RNA so that I could split it multiple times to test each possible point of error on the same set of lysates. Figure 12 shows the results of these experiments, presented as images of SYBR gold stained Urea-TBE gels showing pre- and post-excision.

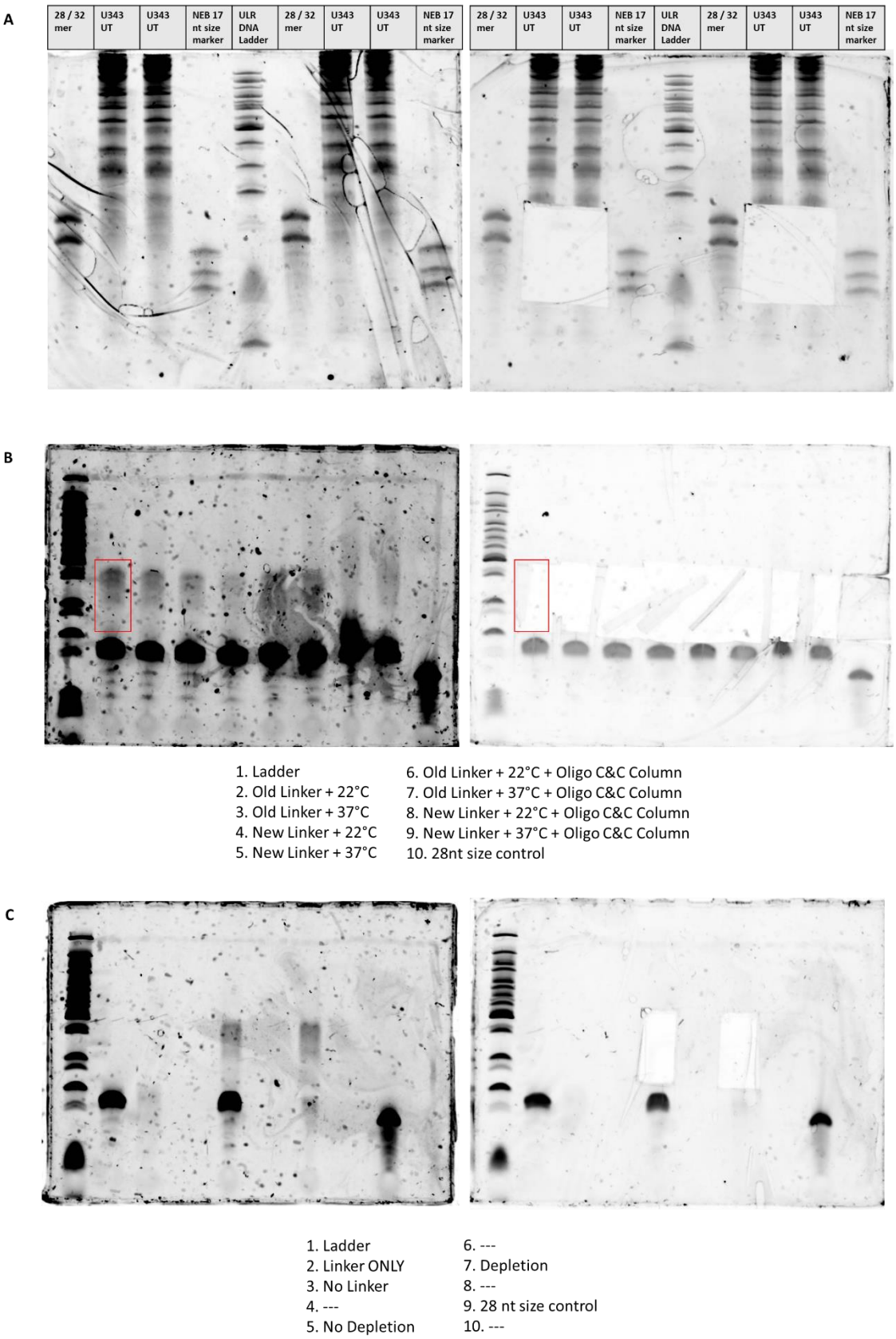

Figure 12. Troubleshooting ligation and RT. All gels were UV-visualized after being

stained with SYBR gold. **a)** Post-centrifugation pellets were purified and separated, 17-34 nt size range was excised. **b)** Excision of ligated fragments and removal of un-ligated linkers. New linkers were created by repeating polyadenylation of the linkers from the same stock. Some samples were cleaned with Zymo Oligo Clean and Concentrator Column following previous gel excision. Temperature shown as the temperature used during ligation for 3 hours at 22 °C or 2 hours at 37 °C. **c)** Following **b)**, RT was performed. Lane 7 used enzymatic depletion of the linker, lane 5 did not. No alterations to the protocol were required and a repeat of the previously used conditions resulted in a bank of the expected size (~105 bp).

After performing the troubleshooting shown in Figure 12, as can be seen in Figure 12c, each of the conditions tested performed as they should, and the error as seen previously was not repeated. Further, the enzymatic depletion as seen in 12c was shown to be effective at removing leftover linker. It is not known what went wrong during the first set of samples when the correct RT product was not seen.

Fortunately, at this point there was no known barriers to performing a full library preparation from start to finish. As a result, I grew up another set of U343 for samples, this time with reverse transfection and TRAIL treatment. As can be seen in Figures 13a and 13b, I ran into no issues in repeating the previous troubleshooted steps and was successfully able to extract an extended band of the correct size. Figure 13a shows the excision of each sample of the 17 – 34 nt as previously described.[50] RNA was then dephosphorylated, ligated, and pooled before RT and enzymatic depletion of un-ligated linkers was performed.

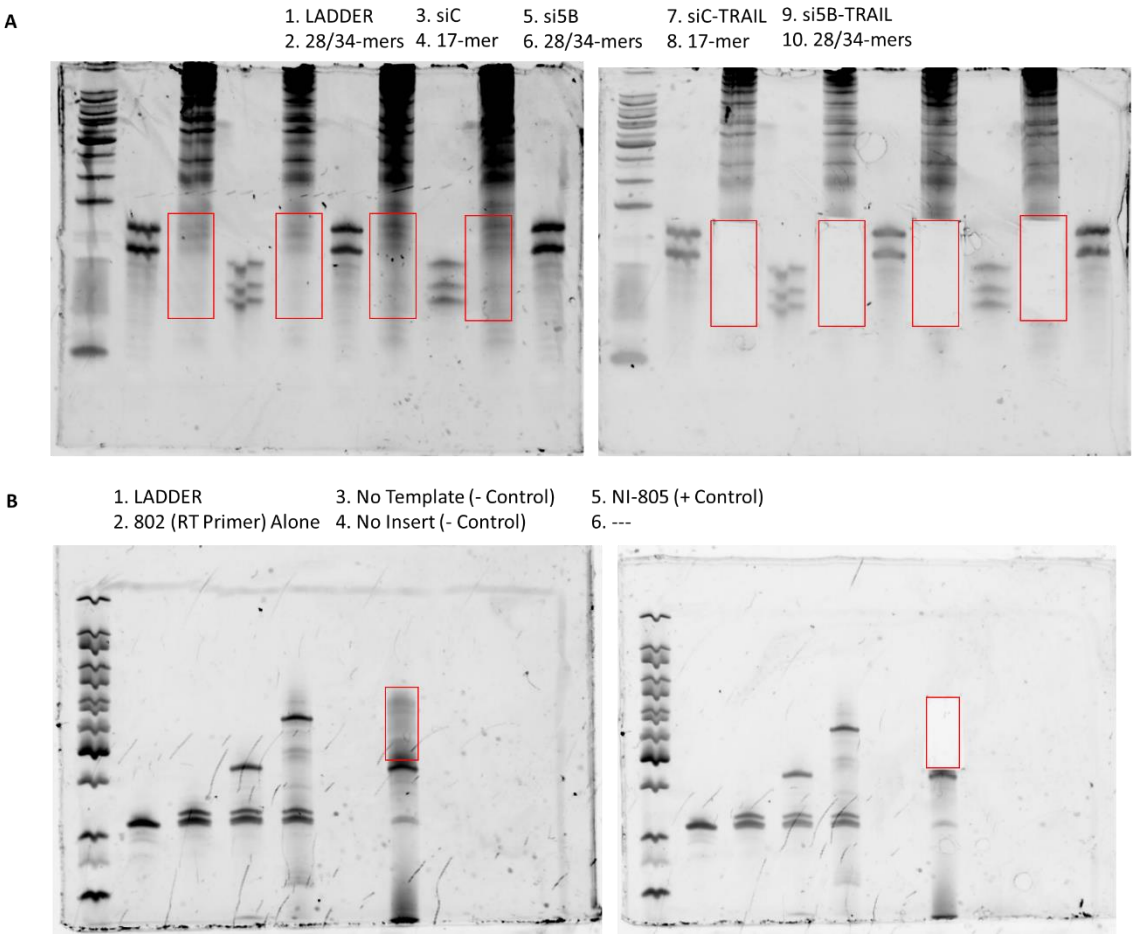

Figure 13. Size Selection and RT product selection. Each gel is UV visualization of SYBR gold stained Urea-TBE gels showing before and after excision. **a)** Size selection gel excising 17 – 34 nt size range. **b)** Excision of RT product selection including any band larger than the linker on its own; ideally one would not cut as close to the empty linker as I did in this image.

The product excised from the RT as shown in Figure 13b was extracted, purified, and ligated with a circ ligase to circularize the product. Following this, 5 µL of the 20 µL circ product was used for further processing. Circ rRNA reduction was performed using biotinylated oligos and streptavidin beads on the sample and was subsequently concentrated and precipitated. A qPCR step was performed on the circ product to determine the concentration – this is used to calculate the optimal number of PCR cycles to perform to

reduce bias for the most concentrated RNA. For replicate 1 (complete set of all four treatment conditions), this was 10 cycles as determined by the table in the reference protocol.[50] Figure 14 shows the excision of the PCR product for replicate 1.

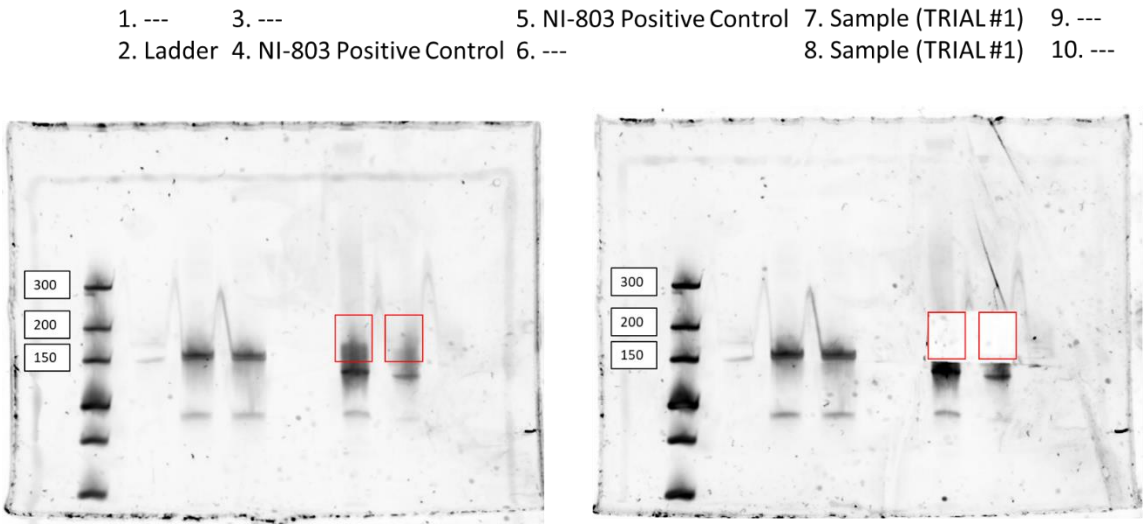

Figure 14. PCR product for Replicate 1. UV visualization of SYBR gold stained Urea-TBE gel. The PCR product equal to and exceeding the height of the control bands was excised and is ready to be sequenced following QC.

Once PCR had been completed, the only steps that remained before it could be sent off for sequencing were quality control (QC) and pooling. Before the QC step was to be performed, however, I prepared PCR products of replicates 2 and 3, as shown in Figures 15 & 16 so that QC could be performed on all 3 replicates simultaneously.

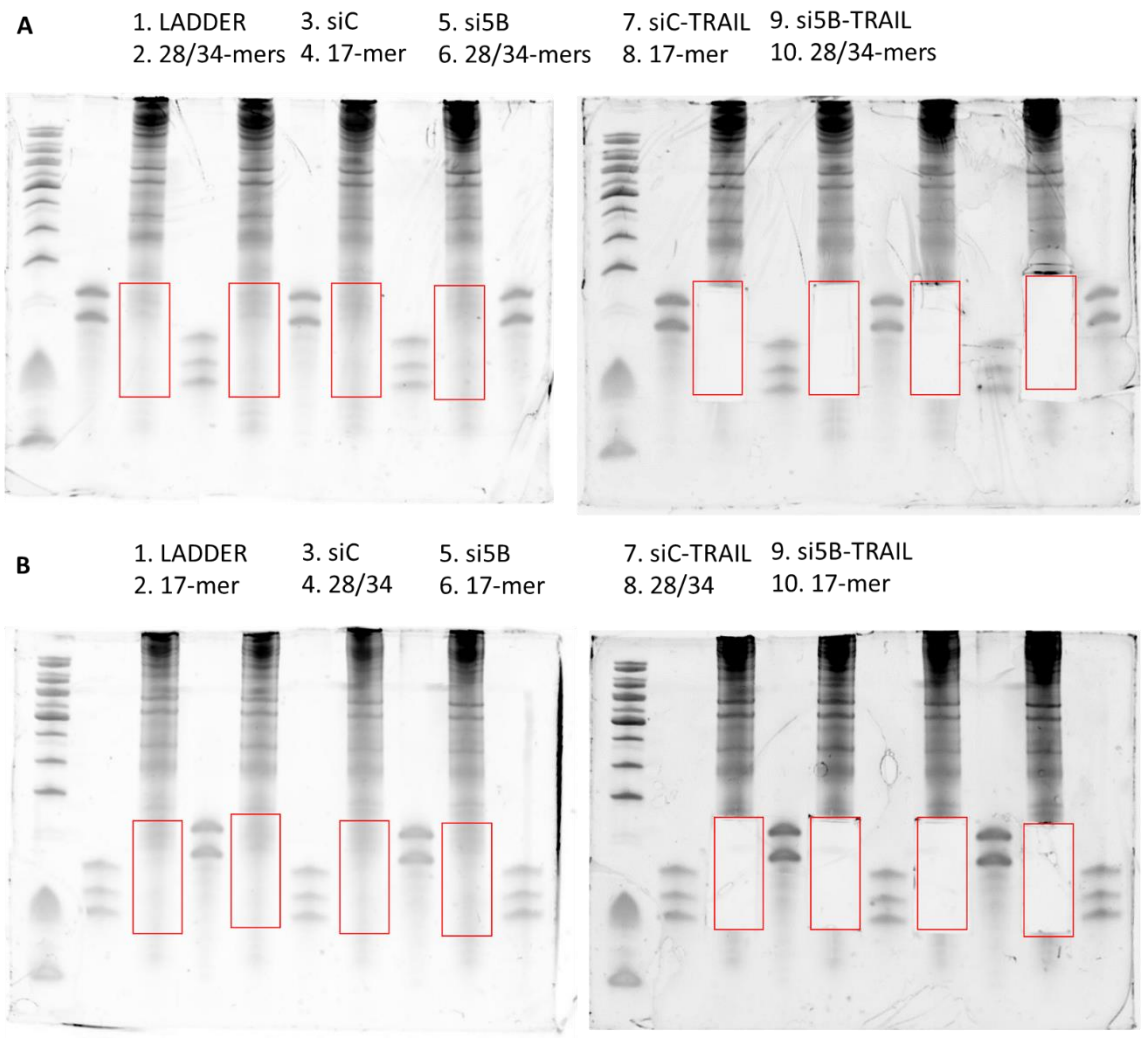

Figure 15. RNA Size selection gels. UV visualization of SYBR gold stained Urea-TBE gels. **a)** Replicate 2. **b)** Replicate 3. Each sample band was excised between 17 nt and 34 nt using the low range ladder and the 34 nt "ladder" as a reference.

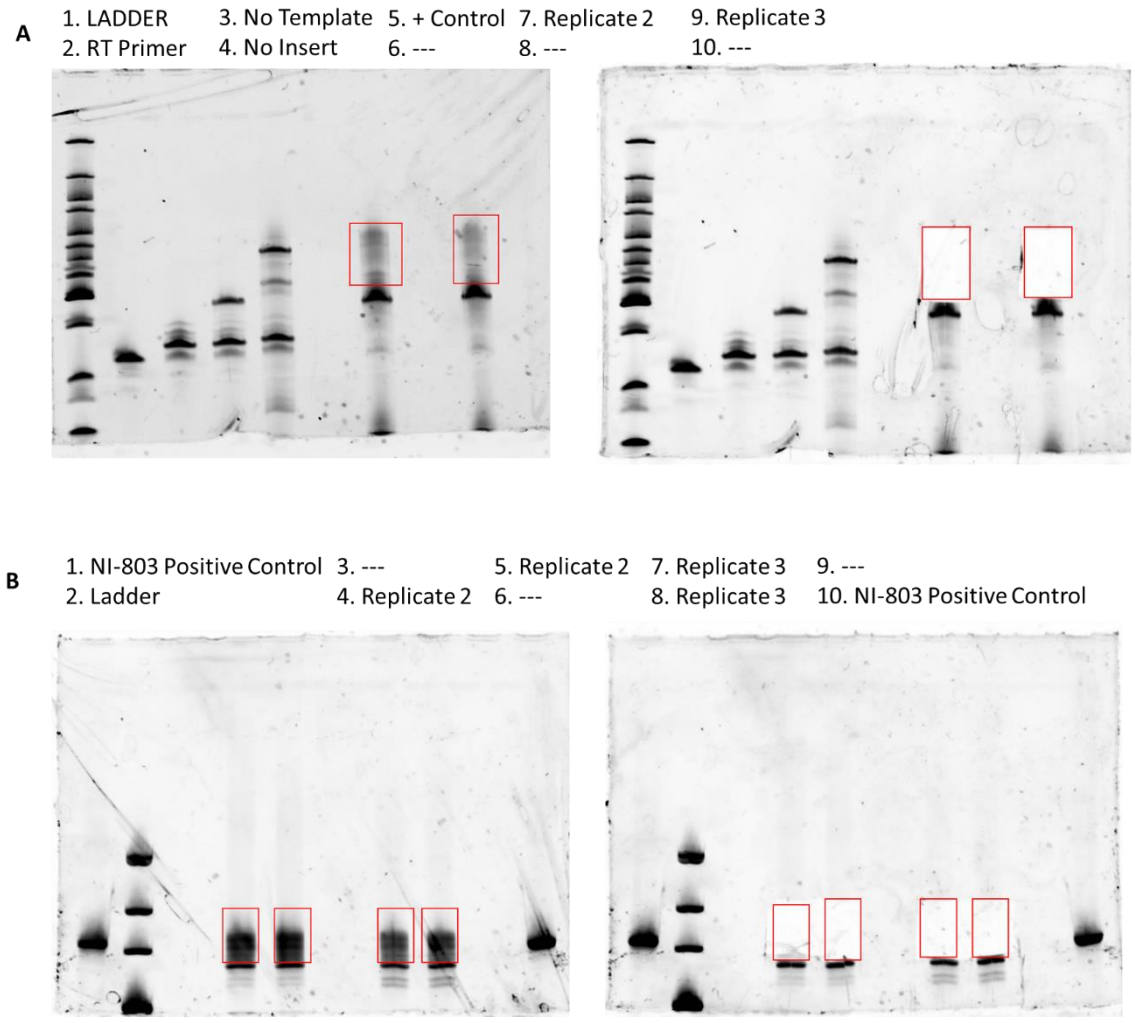

Figure 16. RT and PCR Product Selection Gels. UV Visualization of SYBR gold stained gels. **a)** RT product selection and excision for Replicates 2 & 3 on Urea-TBE Gel. Any fragment greater than the empty linker were excised using the positive control as a reference. **b)** PCR product selection and excision for Replicates 2 & 3 on native-PAGE. Any fragment greater than the empty product was excised. In this example I cut too close to the empty bands in one should be more cautious about retaining any empty vectors.

Once PCR products were produced for replicates 1-3, I performed QC using Agilent's Bioanalyzer on a high sensitivity DNA chip. I used a few different dilution factors, and the 1/5 dilution provided the clearest results. Shown in Figure 17, multiple peaks are visible between 139 – 171 nt. I believe the low peaks around 139-141 nt indicate empty vector contamination. The solution to this would be to excise size selection gels

more conservatively so that no empty vector is collected. Further, having multiple peaks in the 162-170 nt range indicate rRNA contamination; this can be remedied with two possibilities – first, a second round of rRNA reduction could be performed, and second, I could perform multiple PCR preps with fewer cycles and combine the products.

Unfortunately, immediately following QC analysis, before feedback could be collected from my collaborator, I used the remainder of my replicates 1-3 sample lysates to purify RNA for RNA-seq. Each of my generated lysates contains in the range of 450-500 µL of total lysate; of that, approximately 350 µL is used for RFA library generation, and the remaining 150 µL was left in -80 °C for RNA-seq. To purify my RNA from the crude RNA lysate (undigested), I used NEB Monarch total RNA miniprep kit. However, the final elution yielded concentrations which were extremely low and barely registering on the nanodrop. After a series of troubleshooting attempting to recover the RNA, I was unable to convincingly harvest any RNA from column. Using RNA lysate from a previous set of samples, I loaded an equal amount of RNA into both an NEB Monarch total RNA miniprep kit and the other half was purified in a Zymo Directzol RNA miniprep kit. Once again, the NEB kit yielded almost no RNA, whereas the Zymo kit eluted very clean RNA. Ultimately, I am not entirely sure why the samples were incompatible with the NEB kit, possibly due to the lysis buffer I used. Regardless, at this point I had to generate 3 new replicates since the generated libraries were not useful without the RNA from the same initial lysate. Due to the amount of RNA eluted with the Zymo kit in the test sample, two changes were made to fix issues, as well as prevent future issues: I increased the amount of cells seeded for replicates 4-6 by 2x, increasing up to 2x 6-well plates per sample conditions, and additionally I performed a Zymo Directzol RNA miniprep purification immediately after harvesting the RNA lysates before a single freeze thaw. This served the function of ensuring

that I had pure RNA for each sample before spending the time on the RFA library generation, as well as ensuring concentration of each sample was adequate.

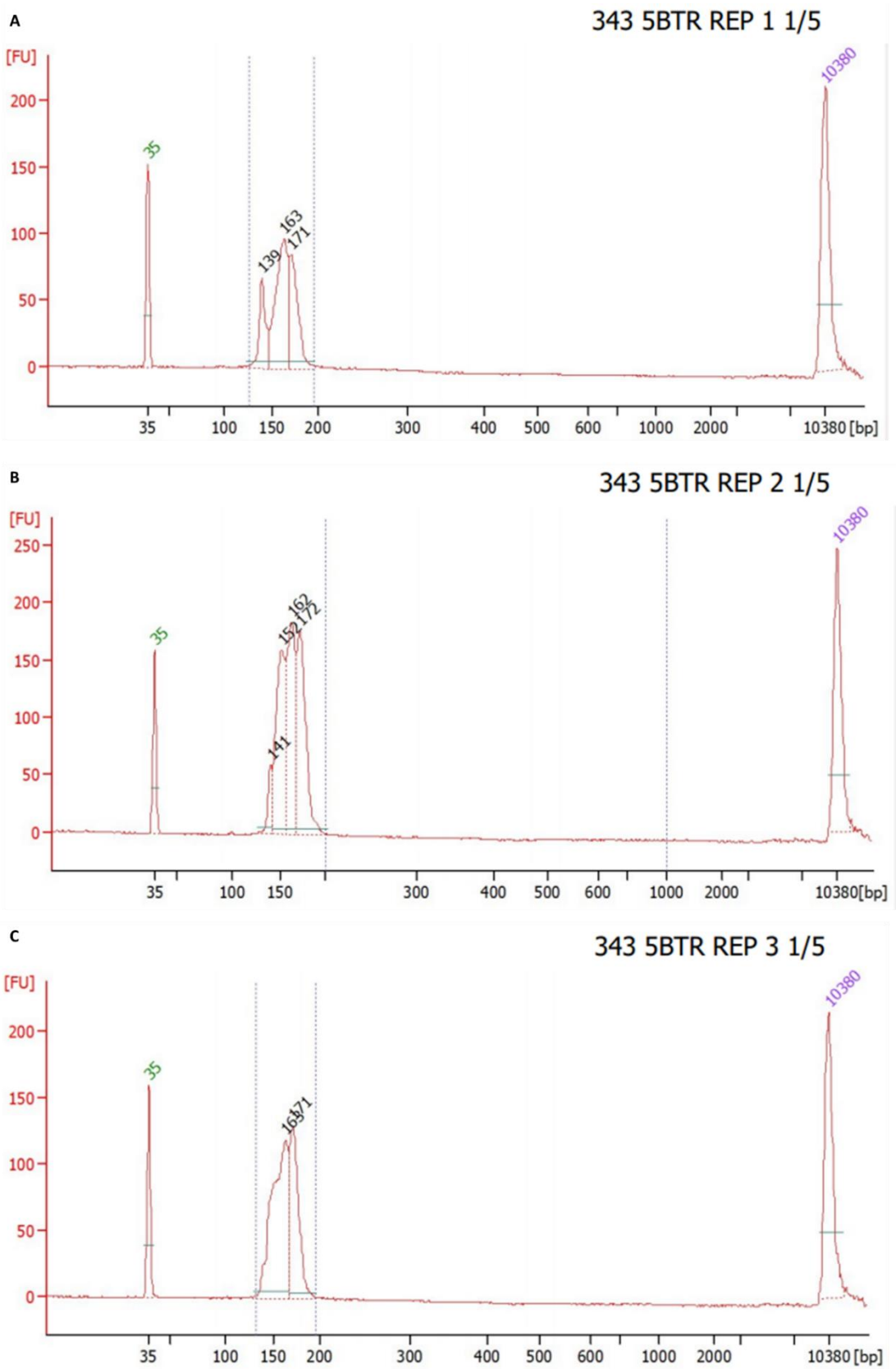

Figure 17. Bioanalyzer QC for Replicates 1-3. Samples were run on High Sensitivity

DNA chip for Agilent Bioanalyzer. Multiple peaks are visible between 130-150, which is an indication of empty vectors and incomplete sequences. Multiple peaks between 150-170 are indicative of dominant sequence contamination; likely ribosomal. Ideally only one dominant sample peak would be present.

Table 1. Concentration and Yield Table for Replicates 4-6. RNA concentrations and yields from replicates 4-6. ******* Replicate 5 siC sample was spilled loading into the ultracentrifuge, so a new sample, Replicate 7 siC was prepared and centrifuged along with replicate 6.

Sample	[ug/mL] Lysate	[ug/mL] Directzol	Elution volume (uL)	ug Pure RNA
(4) siC	75.57	132	25	3.04
(4) si5B	89.33	184.8	25	4.25
(4) siC + TRAIL	56.71	197.4	25	4.54
(4) si5B + TRAIL	147.9	295.6	25	6.80
(5) siC ***	46.4	74.18	50	3.56
(5) si5B	56.48	78.9	50	3.79
(5) siC + TRAIL	94.74	87.71	50	4.20
(5) si5B + TRAIL	145.7	164.2	50	7.88
(6) siC	192.7	70	50	3.36
(6) si5B	156.6	86.54	50	4.15
(6) siC + TRAIL	114.8	78.34	50	3.76
(6) si5B + TRAIL	156.8	99.58	50	4.78
(7) siC	185.1	193.9	50	9.3

Replicates 4, 5, and 6 were harvested from two 6-well plates per sample condition. When an old lysate was tested using Zymo Directzol RNA miniprep, 100 µL of lysate yielded only 1.5 µg of RNA, whereas 3-5 µg would be preferable. As can be seen in table 1, all samples collected in replicates 4-6 contained at minimum 3 µg of pure RNA was collected from each sample. However, this increase was not achieved just from doubling the amount of starting material. Due to doubling the amount of cells being lysed, lysis became less efficient and some minor adjustments had to be made to improve upon the previous lysis protocol. Time on ice was increased from 30 minutes to 40 minutes and a step triturating each sample with a 21G needle was effective at breaking up the mucous-like clump that formed during lysis.

RFA preparation was performed as previously with no protocol changes in the first few steps. Figure 18 shows size selection excision; however, unlike the previous replicates, due to Covid-19 concerns and the university closure, the excised samples were extracted, precipitated, and kept at -80 °C for 3.5 months due to University closure. Upon reopening, samples were dephosphorylated, the linker was ligated, and samples were pooled as previously described. Following this, reverse transcription was performed on replicates 4, 5, and 6. Shown in Figure 19, replicate 4 was completely degraded with no sign of a band at the expected size, whereas replicates 5 and 6 both displayed extension at the expected size, with replicate 5 present at a lesser concentration than replicate 6. As a result of the lack of a visible band in replicate 4, sample preparation was only continued with replicates 5 and 6.

To avoid the rRNA contaminants which were present in the previous round of replicates bioanalyzer step, prior to qPCR quantification, two rounds of rRNA subtraction were performed, in contrast with the previous single round of rRNA subtraction. These were performed on two separate days with a long O/N precipitation step in between. Additionally, as a further measure to reduce rRNA contamination, after calculating the ideal number of PCR cycles to be 11 cycles, PCR was performed with only 10 cycles in stead. To increase the amount of product, two tubes were used for each replicate with a reduced cycle number and pooled during the PCR size selection gel. Figure 20 shows the PCR size selection as well as one further variance from the previous replicates – in this PCR gel, bands of the correct size were meticulously cut so as to not include empty vectors by ignoring the smaller band and being more specific with excision.

Following PCR product selection and excision, gel slices underwent DNA extraction as previously described, samples were precipitated O/N at -20 °C and were

stored at -20 °C. Finally, quality control was performed on an Agilent Bioanalyzer High Sensitivity DNA Chip at a dilution factor of 1:5. As can be seen in Figure 21, in contrast with replicates 1-3, one dominant peak is clearly seen of the expected size. There remains some minor empty vector contamination, however, this makes up only approximately 5% of the total sample, as well as none of the visible rRNA contaminants that were previously present in replicates 1-3. Due to time constraints and RNA integrity concerns due to sitting for so long, the samples will not be sent off for processing. However, the difference between the previous Bioanalyzer results and these most recent ones demonstrates the level of optimization that has occurred, and that RFA library preparation done with U343 in our lab has been successfully established and optimized from start to finish.

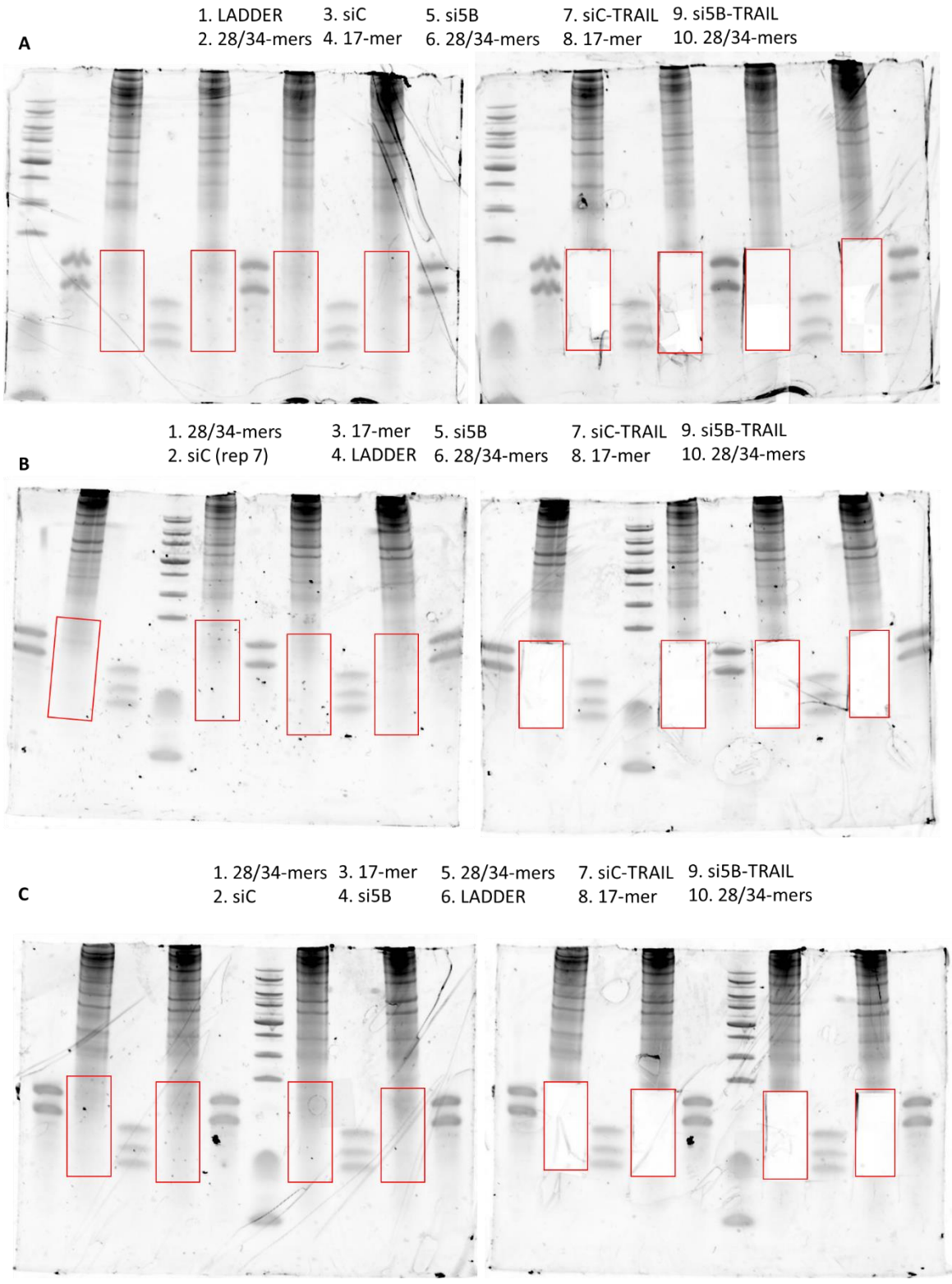

Figure 18. Size Selection Gels Replicates 4-6. UV-visualization of SYBR gold stained Urea-TBE gels. **a)** Replicate 4. **b)** Replicate 5. **c)** Replicate 6. Each sample band was excised between 17 nt and 34 nt using the low range ladder and the 34 nt "ladder" as a reference.

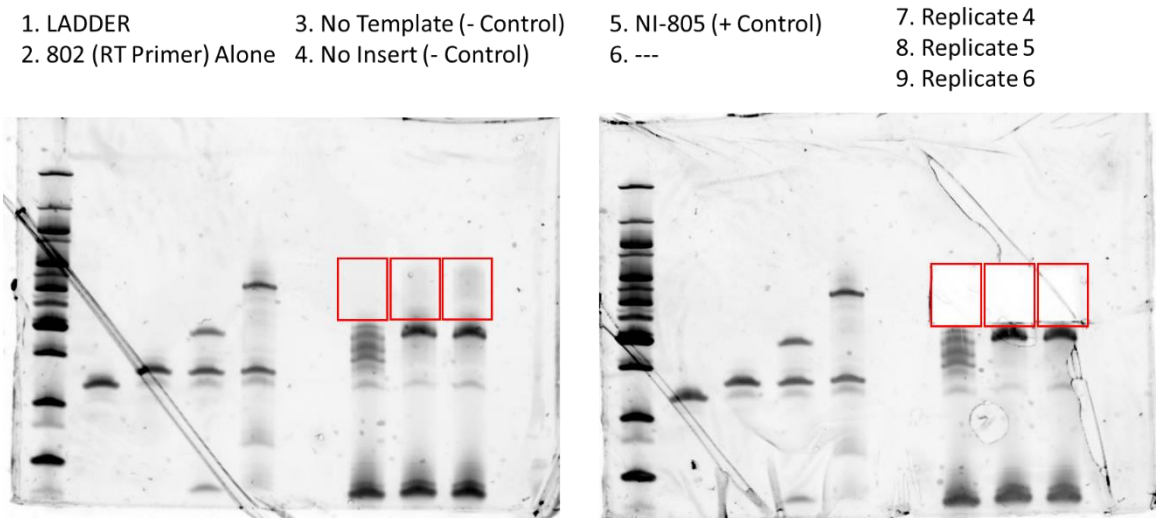

Figure 19. RT product size selection Replicates 4-6. UV-visualization of SYBR gold stained Urea-TBE gels. Any band product greater than the empty linker band product at ~75 bp was excised. Replicate 4 (lane 7) has indicators of RNA degradation and was not used for further steps.

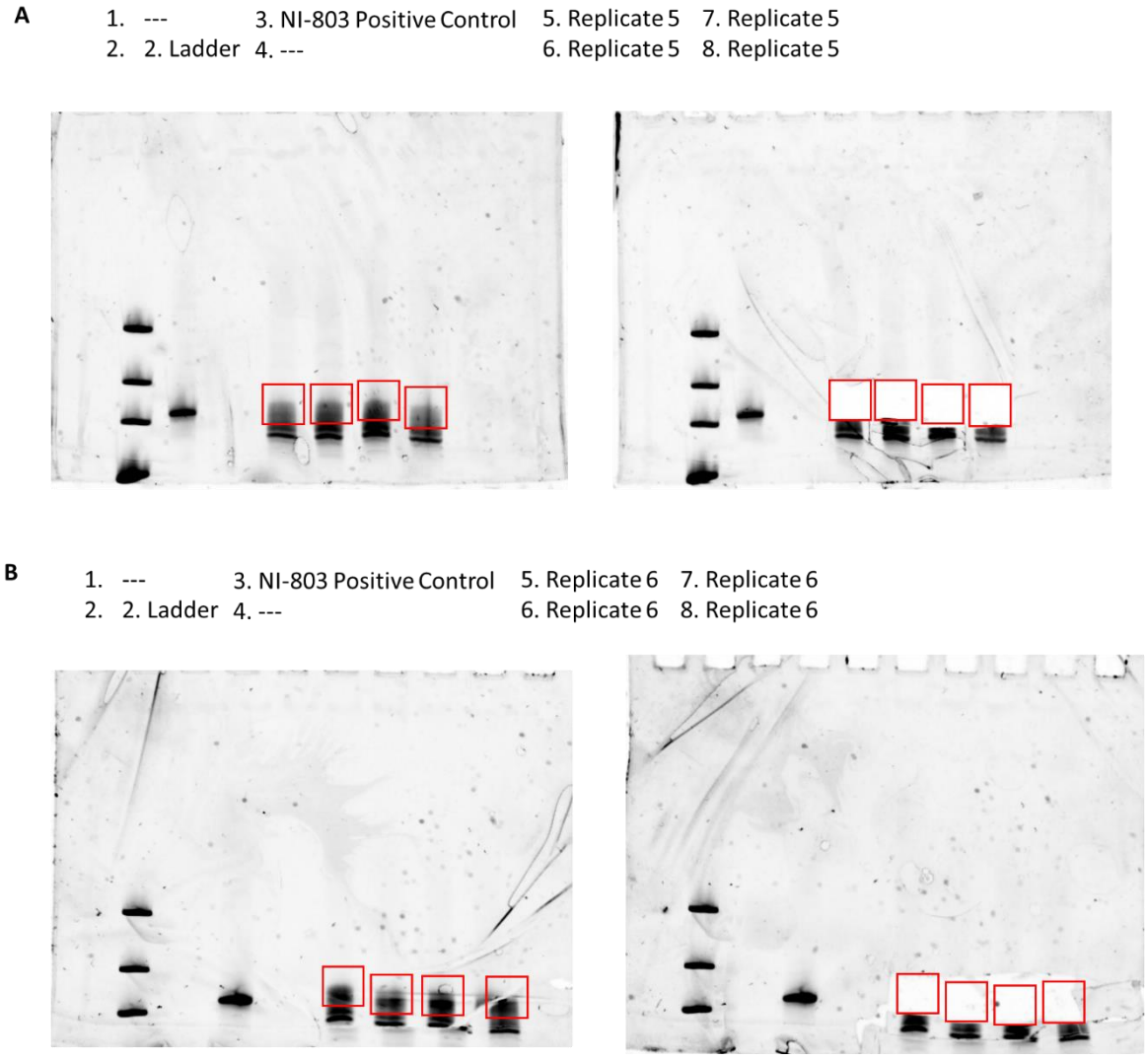

Figure 20. PCR Product Size Selection Replicates 5 & 6. UV-visualization of SYBR gold stained native-PAGE gel. Any sample significant above the empty vector band as demonstrated in the above images was excised.

A

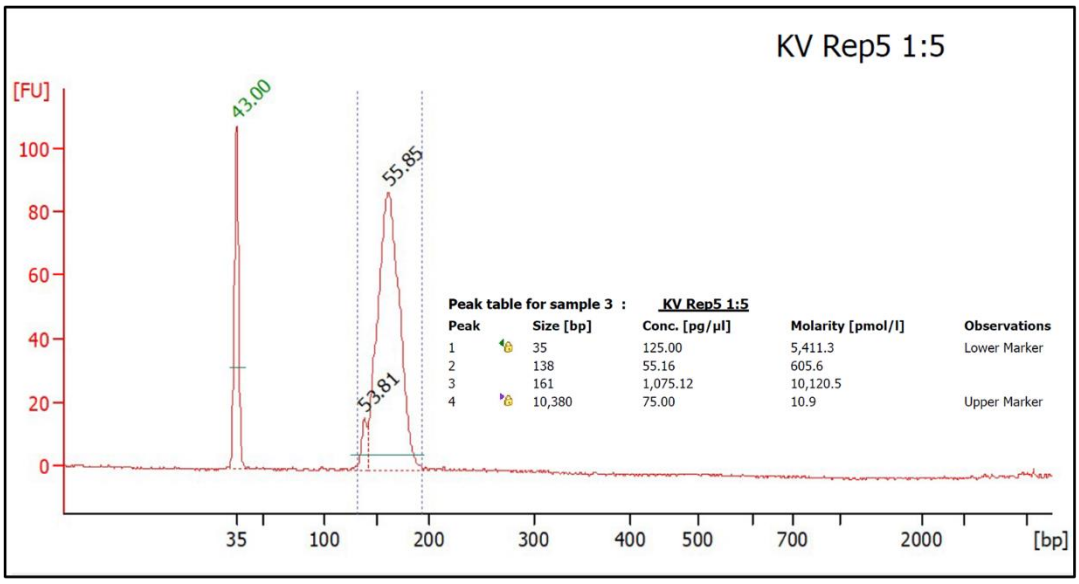

B

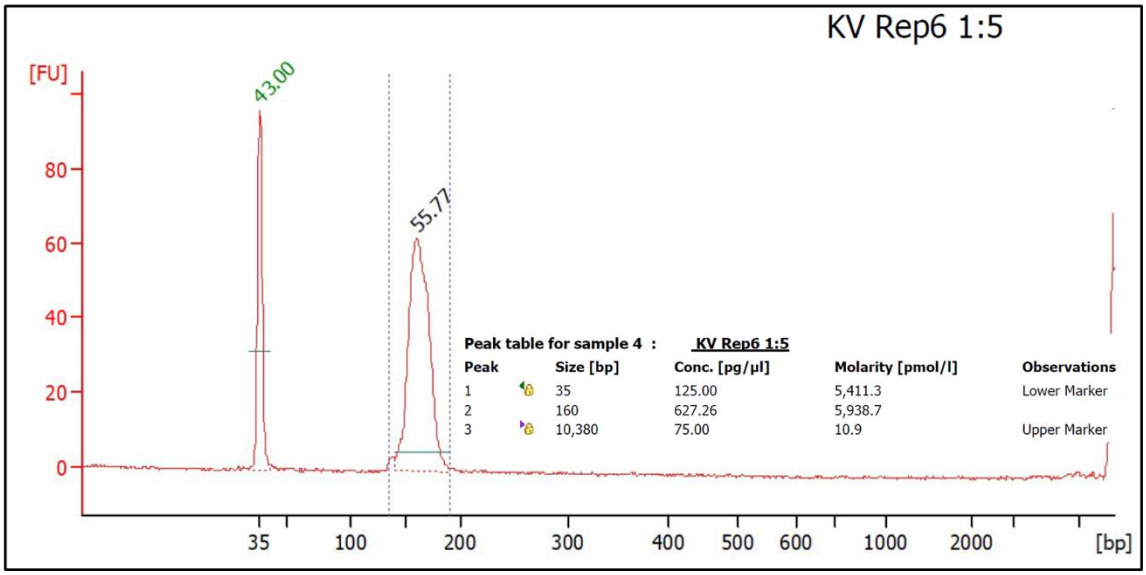

Figure 21. Bioanalyzer QC for Replicates 5 & 6. Samples were run on High Sensitivity DNA chip for Agilent Bioanalyzer. Each replicate displays one dominant peak as desired; however, replicate 5 does contain a small empty vector contamination peak.

4 Discussion

4.1 Metabolomics

Of the metabolites which were differentially expressed, there is a shorter list of metabolites which displayed robust and definitive differential expression. Those metabolites include creatine, phosphocreatine, *myo*-inositol (MI), o-phosphocholine, fumarate, and UDP-N-acetylglucosamine. These metabolites represented the most robust differences between the si-Control + TRAIL and the si-eIF5B + TRAIL samples. Specifically, compared to the control + TRAIL samples, creatine, phosphocreatine, fumarate, and *myo*-inositol were greatly increased, whereas o-phosphocholine, and UDP-N-acetylglucosamine were present at lower concentrations in the si-eIF5B + TRAIL samples.

4.1.1 Myo-Inositol

Multiple of these metabolites have direct cancer relevance, and *myo*-inositol is of interest for a few reasons, but this interest is predominantly driven by a greater than two-fold increase in concentration under conditions of eIF5B depletion in both the untreated and TRAIL treated si-eIF5B samples. Inositol is a group of carbocyclic sugar alcohols, with *myo*-inositol being the most prominent isomer. *Myo*-inositol is synthesized naturally in both animal and plant tissues and plays an important role in secondary messaging in its phosphorylated and lipid forms – inositol triphosphate (IP_3) and phosphatidylinositol phosphate lipids (PIP_2/PIP_3) respectively.[62] *Myo*-inositol used to be regarded as an essential nutrient, however, more recent research does not classify it as one due to the fact that it is produced in sufficient quantities from D-glucose. M*yo*-inositol in its free form is readily

available as either phosphoinositides or phytic acid (IP_6) – the primary storage method of phosphorous in plant tissues, so some combination of synthesis and uptake is generally responsible for the presence of MI in cells. Interestingly, *myo*-inositol is an essential nutrient for human cell culture as well as required for fetal development in both hamsters and mice.[63]

There are three primary ways that cells obtain their MI: biosynthesis from glucose-6-phosphate (G6P), uptake from the surroundings, and dephosphorylation of inositol phosphates. As mentioned, *myo*-inositol is an essential component of DMEM, however, I have not tried to grow cells in a *myo*-inositol-free medium. *Myo*-inositol can be synthesized in rat testis, kidney, liver, and most notably – brain tissues.[64] MI frequently accumulates in brain tissues at greater concentrations than other tissue types in part due to increased expression of the sodium-dependent *myo*-inositol transporters 1 and 2 (SMIT1 / SMIT2) as well as the H^+ cotransporter HMIT. Beyond uptake, however, brain tissues can synthesize *myo*-inositol through multiple pathways: *de novo* biosynthesis of *myo*-inositol from G6P with the help of Inositol-3-phosphate synthase 1 (INO1) and *myo*-inositol-1-monophosphatase (IMPA), or through various phosphatases which restore inositol phosphates (IPs) to *myo*-inositol. MI has many uses in the cell and is therefore regulated through a multitude of mechanism and pathways, some of which are abused or regulated in cancer cells such as astrocytomas.

Patients with grade II (A-II) astrocytomas expressed consistently higher levels of *myo*-inositol than their grade IV, or glioblastoma (GBM), counterparts did.[65,66] Further, MI levels trended downwards from A-II to GBM including in grade III astrocytomas (A-III).[66] In that same study, the authors find that (mI + glycine) / (Creatine) levels represent an accurate method for astrocytic tumour grading; however, they do express caution and

recommend combination with other techniques due to lack of NMR visibility for glycine.[66] In my metabolomic analysis, I found robust increases in both creatine and *myo*-inositol when eIF5B was knocked down. Notably, my analysis was performed on U343, a GBM cell line, which is noted to have a phosphatase and tensin homolog (PTEN) mutation according to an analysis from the Broad Institute.[67] PTEN mutations are associated with decreased levels of *myo*-inositol and creatine, as well as increased levels of glycine.[68] In fact, according to the Catalogue Of Somatic Mutations In Cancer (COSMIC), 50% of sequenced GBMs contained PTEN mutations – however, this can not be used on its own to extrapolate any information due to the fact that A-II cell lines have a 54% rate of PTEN mutations.[69] PTEN is a tumour suppressor gene which encodes phosphatidylinositol-3,4,5-triphosphate 3-phosphatase.

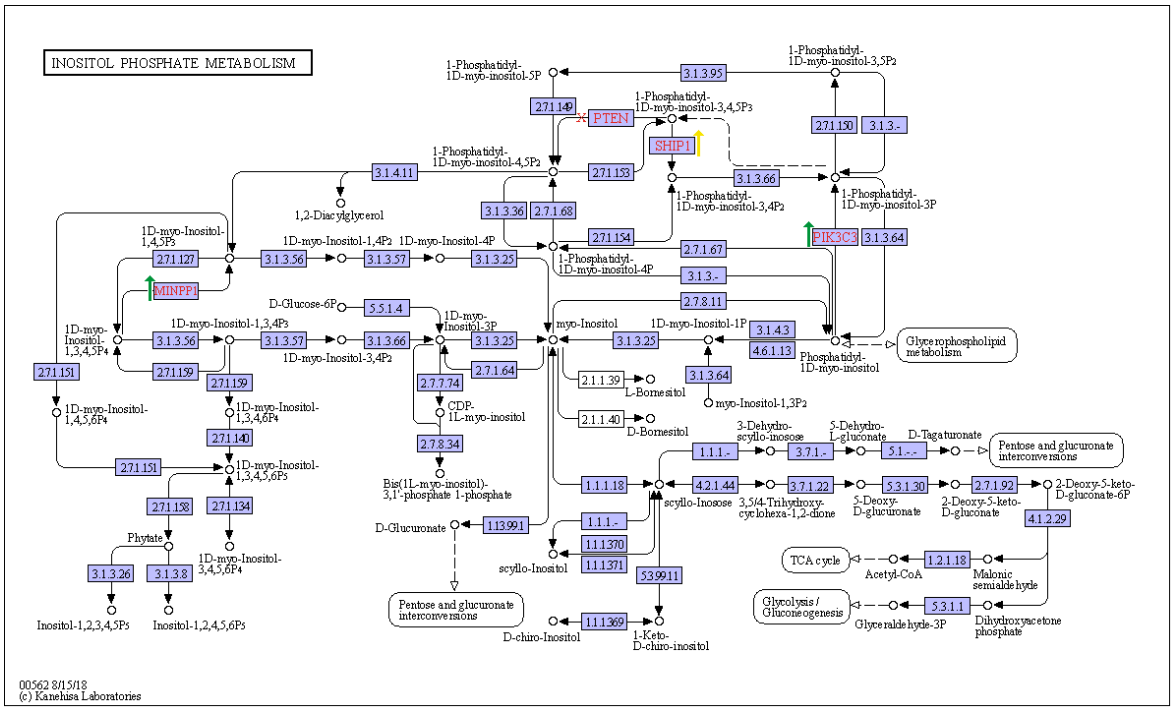

Figure 22. Inositol Phosphate Pathway from KEGG. Green arrows are upregulated at the protein level upon eIF5B depletion in Jiang et al's data, yellow arrow is upregulated at the transcriptional level upon eIF5B depletion in Bressler's data, and the red X represents a mutation losing gene function.[70,71]

PTEN and phosphatidylinositol-4,5-bisphosphate 3-kinase (PI3K) play opposing roles in the conversion between phosphatidylinositol-3,4,5-triphosphate (PIP_3) and phosphatidylinositol-4,5-bisphosphate (PIP_2).[72] In U343 specifically and as many as 50-80% of sporadic cancers include loss-of-function PTEN mutations which lead to unregulated PI3K signaling.[72] PI3K is regulated by growth factors through receptor tyrosine kinases (RTKs) such as the EGF receptor family, VEGF receptor family, and the HGF receptor family.[73] Following activation by PI3K, PIP_3 recruits Akt through it's plekstrin-homology (PH) domain and localises to the cell membrane where it regulates a large set of pro-survival targets and pathways.[72] Due to the PTEN mutation in U343, PIP_3 is not converted back to PIP_2 and Akt signalling is allowed increase.

Currently unpublished data collected in our lab demonstrate that many GBM cell lines, U343 included, constitutively express greater levels of eIF5B when compared to healthy brain tissues. Based on the translatomic and transcriptomic and data generated by Jiang & Bressler, when depleted of eIF5B he PI3K-Akt signalling pathway is affected at multiple levels through various proteins. In a recent RNA-seq performed on HEK 293T cells in the presence and absence of eIF5B, it was found that SHIP1 was significantly upregulated at the transcriptional level when eIF5B was depleted.[74] As shown in Figure 22, SHIP1 is a phosphatase responsible for the conversion of PIP_3 to phosphatidyl-3,4-bisphosphate. Notably, although this molecule is a different form of PIP_2, it cannot be converted back into PIP_3 by PI3K – which allows SHIP1 to counteract the effects of PI3K and decrease Akt signalling. Following dephosphorylation by SHIP1, phosphatyidyl-3,4-bisphosphate is dephosphorylated once more into phosphatidylinositol 3-phosphate (PtdIns3P) by INPP4. Also performed in HEK293T, a recently published proteomics analysis in the presence and absence of eIF5B found mild but significant 1.3x increase in

the protein levels of PIK3C3.[70] Not to be confused with PI3K, which is made up of the catalytic subunits A,B, and D, PIK3C catalyzes the conversion of phosphatidylinositol (PtdIns) into PtdIns3P as seen in Figure 22. PIK3C3 is also known as VPS34, a class III PtdIns 3-kinase and is the enzyme principally responsible for generation of PtdIns3P.[75] Notably, unlike its triphosphate counterpart, PtdIns3P does interact with the PH domain, and so cannot activate Akt; however, PtdIns3P does bind to both FYVE domains as well as a PX domains.[76] Notable proteins which bind to PtdIns3P include sorting nexin 1 (SNX1), hepatocyte growth factor-regulated tyrosine kinase substrate (HGS), and early endosomal antigen 1 (EEA1).[77,78]

Of these, one of special interest is HGS, previously called Hrs, a FYVE domain-containing protein which also binds to ubiquinated EGFR and is required for EGFR sorting and localization to ILV's for exosome formation.[79] Further, PtdIns3P itself plays an essential role in the movement of EGFR through endosomal and the lysosomal pathways.[75,79] We recently published a paper demonstrating a reduction in EGFR under conditions of eIF5B depletion and TRAIL treatment, as well as a reduction in P-EGFR under conditions of eIF5B depletion.[15] Under identical conditions we did not see an associated decrease in Akt or P-Akt under conditions of eIF5B depletion at the protein level, and notably, Jiang *et al.* did not see a change in SHIP1 in their proteomic analysis, indicating that while we did see an increase in mRNA concentration, it may not be reflected at the protein level.[70] The antibody used to visualize the western blots for Akt detects all 3 isoforms, and the antibody for P-Akt also detects all 3 isoforms at their respective phosphorylation sites (Cell Signalling Tech, 9272/9271). Due to the reported non-redundant functional roles of each Akt isoform, it would be interesting to look into differential expression and activation of each one.[80] Nonetheless, Akt is not the only target

regulated by variation in levels of various PtdIns: PI3K-dependent serum and glucocorticoid-regulated kinase (SGK3), a PX domain containing protein, is involved in the regulation of a variety of cell growth, proliferation, migration, and survival pathways.[80] PtdIns3P binds to and activates SGK3 on the endosome, which encompasses a set a complex of interactions, some of which are partially dependent on class I PI3Ks, and some of which appear to be PI3K-independent.[80]

4.1.2 Creatine

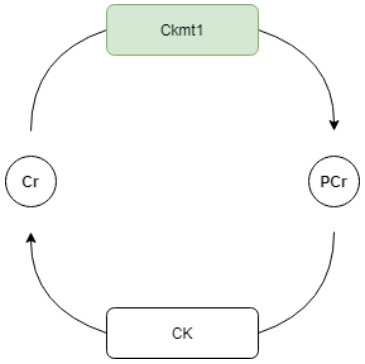

Figure 23. The Creatine / Phosphocreatine Cycle. Metabolites creatine and phosphocreatine shown as circles, enzymes Ckmt1 and CK shown as rounded rectangles. Enzymes shown in green were shown to be upregulated at the protein level in Jiang et al's data.[70]

Creatine and phosphocreatine are closely involved with multiple cancers, and has been studied specifically with regards to HER2 activity and breast cancers.[81] Creatine and phosphocreatine are converted between each other by two primary enzymes: mitochondrial creatine kinase 1 (Ckmt1), a mitochondrial protein, facilitates the conversion of creatine into phosphocreatine, and cytosolic Cr kinase (CK) which converts phosphocreatine back into creatine. Notably, this mechanism is utilized by cells under conditions of stress and energy demand to quickly produce ATP through the conversion of phosphocreatine into

creatine.[81] As can be seen in table 2, when the cells were depleted of eIF5B, I saw a greater increase in phosphocreatine than creatine, which corresponds closely with data shown by Jiang *et al* which saw a 1.7x increase in Ckmt1 protein expression when eIF5B was depleted.[70]

Table 2 metabolite expression set compared to siC samples as 100%

	si-Control	siC + TRAIL	si-eIF5B	si5B + TRAIL
Creatine	100	71.3	113.0	140.9
Phosphocreatine	100	53.8	138.9	72.4

Under conditions of TRAIL treatment both si-control and si-eIF5B samples expressed a significant decrease in the amount of phosphocreatine detected. This is to be expected, as under conditions of TRAIL treatment the cells are surely in need of fast energy. This does not, however, help explain the increased sensitivity U343 cells show towards TRAIL treatment under conditions of eIF5B depletion. In fact, downregulation of Ckmt1 has been shown to have a negative effect on cell proliferation in cell lines with elevated HER2 expression.[81] On a related note, HER2 (ERBB2) protein expression was elevated following eIF5B depletion in the proteomics data provided by Jiang *et al*.[70] Therefore, while this data correlates with other published materials, it does not lend itself as one of the potential mechanisms by which eIF5B sensitization occurs.

4.1.3 O-phosphocholine

Regulation of choline metabolism and subsequent misregulation are commonly considered as hallmarks for oncogenesis.[82-84] Choline metabolism activation is signified by increases in phosphocholine (PCho) and total choline-containing compounds (tCho) and can be the cause or effect of many tumorigenic pathways and systems. Notably, malignant transformation and specific tumour microenvironment seem to associate with increased PCho expression – in one example, transferring media from cultured cancer cells increased PCho concentrations when used to culture healthy cells.[82] In my data, I see general decreases in choline across the board under eIF5B depletion, and notably significant decreases in PCho levels under both eIF5B depletion and TRAIL treatment individually, as well as further increases under combined treatment. Other authors have pointed out the difficulty in properly separating the levels of choline, phosphocholine, and glycerophosphocholine (GPCho) due to peak overlaps when utilizing ^{1}H MRS (NMR); however, while they do express this concern, they do claim that cancer cell extracts such as those I prepared should have enough resolution to differentiate, whereas live cancer cells and tumour models do not contain enough resolution to differentiate.[82] When combining their analysis demonstrations and using the peaks in the 3.20 - 3.24 ppm range to quantify relative levels of choline, phosphocholine, and glycerophosphocholine levels I get quite interesting trends as seen in table Y.

Table 3. metabolite expression set compared to siC samples as 100%

	si-Control	siC + TRAIL	si-eIF5B	si5B + TRAIL
Choline	100	93.6	90.2	141.7
Phosphocholine	100	58.2	36.0	26.0
Glycerophosphocholine	100	87.0	55.1	51.6

As can be seen in table Y, choline concentrations seem to increase specifically only under conditions of eIF5B depletion and TRAIL treatment, phosphocholine levels seem to decrease significantly under TRAIL treatment, and even further under si-eIF5B and combined treatment. Glycerophosphocholine, on the other hand, decreases slightly under TRAIL treatment, but much more drastically under eIF5B depletion. Notably, GPCPD1, an enzyme responsible for the conversion of glycerophosphocholine to choline shows decreased protein expression under conditions of eIF5B deletion.[70] While this information does not directly support the decrease in glycerophosphocholine we see under removal of eIF5B, we do not see a corresponding increase in choline under eIF5B treatment alone, which one would expect to correlate with decreases in glycerophosphocholine if those differential expressions did revolve around GPCPD1.

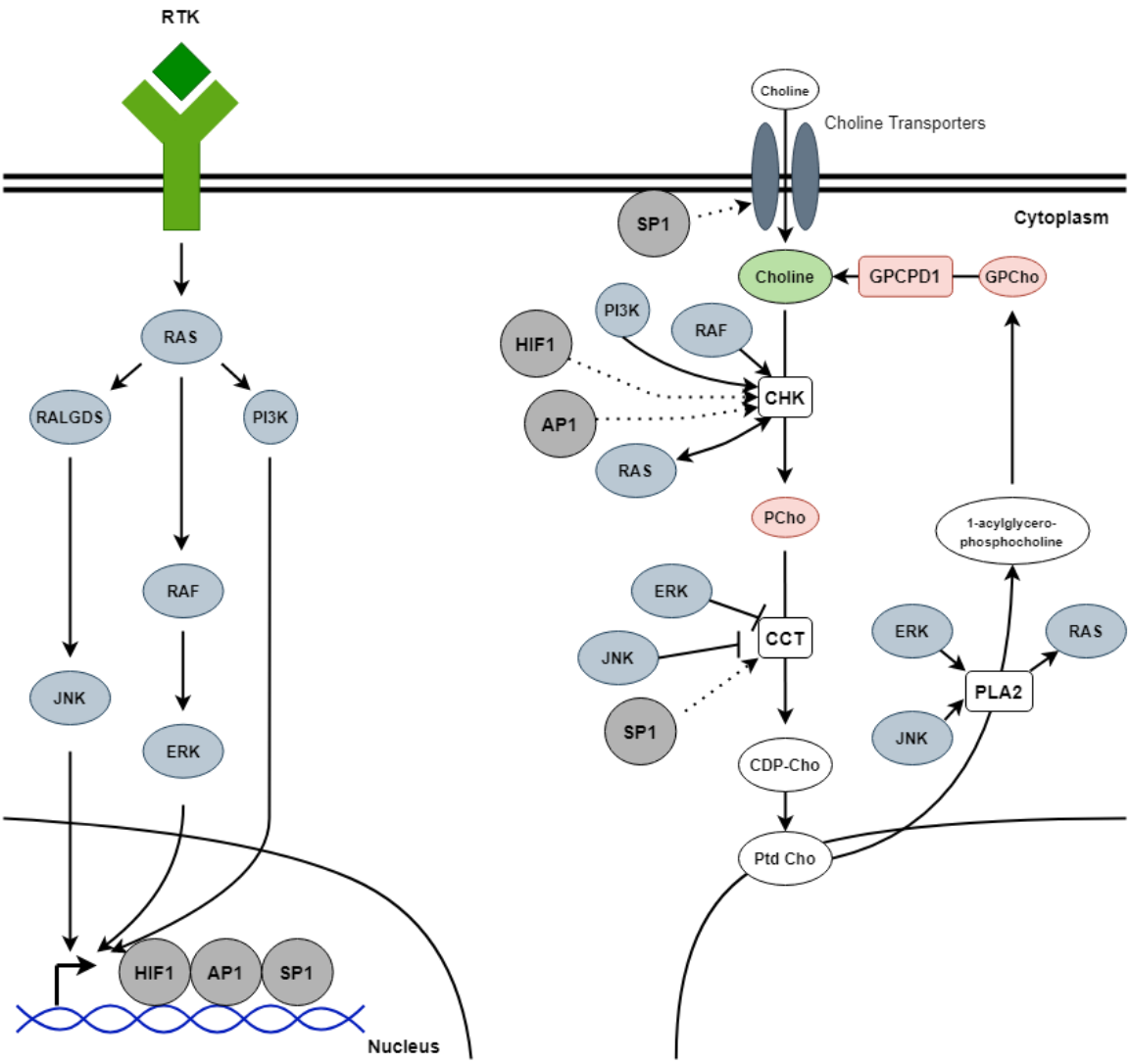

Figure 24. Interaction between the RTK pathway and Choline. The left side of the Figure shows RTK-activated pathways which result in the transcriptional upregulation of the proteins shown as dark red in the right panel. The right panel shows the relationship between various choline compounds and how they are converted between themselves. Metabolites shown in red were present at lower levels in eIF5B + TRAIL and metabolites shown in red were present at higher levels in eIF5B + TRAIL. Enzymes shown in red showed decreased protein expression in Jiang et al's data.[70]

Choline metabolism is tightly intertwined with RTKs through RAS and PI3K which through their signalling pathways increase expression of HIF1, AP1, and SP1.[82] Through these proteins, PI3K, RAS, RAF, ERK, and JNK regulate the choline metabolism at multiple different points such as choline kinase (CHK), CTP:phosphocholine cytidyltransferase (CCT), and phosphatidylcholine-specific phospholipase (PLA2). These

enzymes in return control the conversion of choline to phosphocholine (CHK), from phosphocholine to the high-energy intermediate cytidine diphosphate (CDP)-choline (CDP-Cho), and from phosphatidylcholine to acylglycero-phosphocholine – the precursor before GPCho – by PLA2.[82] According to a data table provided by Glunde *et al* containing relative concentrations of cholines in various tissue types, for brain tissues, levels of PCho and total choline were greatly elevated in cancer vs. noncancer, whereas GPCho concentrations were typically down slightly relative their non-cancerous counterparts in the brain. Interestingly, choline kinase α (CHKA) has been shown to co-immunoprecipitate along with EGFR in a variety of breast cancer cells lines, and interacts quite closely along with EGFR signalling.[85] In fact, EGFR overexpression was shown to increase total activity and expression of CHKA; consequently, depletion of CHKA resulted in a decrease in EGF-dependent cell proliferation. The authors suggest this is link exists as a c-Src-dependent interaction between EGFR and CHKA – in the absence of c-Src kinase activity this EGFR-CHKA interaction was not immunoprecipitated, and that the kinase activity of c-Src, not EGFR, was important fort CHKA activity.[85]

4.1.4 Fumarate

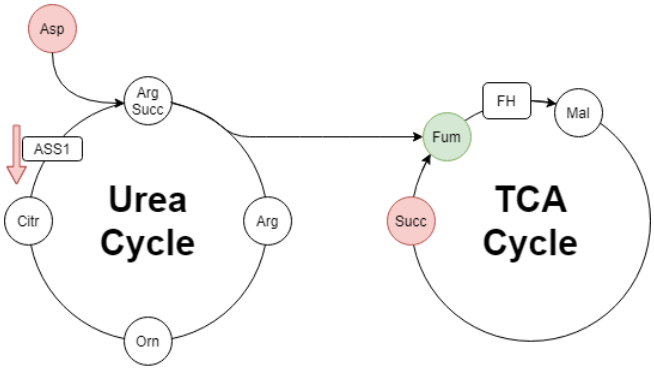

Figure 25. Fumarate in Relation to the Urea and TCA Cycles under si5B + TRAIL Treatment. Metabolites shown as circles, enzymes ASS1 and FH shown as rounded rectangles. Metabolites are colour coded based on whether they were up (green) or down (red) under conditions of both si5B and TRAIL treatment relative to the control treatment. Enzymes shown with a red arrow were shown to be downregulated at the protein level in Jiang et al's data.[70]

The urea cycle, involved in arginine biosynthesis, is another example of a pathway altered by the depletion of eIF5B. Within the pathway, aspartate and fumarate are significantly differentially regulated while it is unclear whether the other metabolites were affected greatly. Ornithine is also potentially differentially regulated; however, it lacks a single clean peak so it is difficult to comment on its relative concentrations. Upstream of urea production, aspartate is converted into arginosuccinate by arginosuccinate synthase (ASS1). Under conditions of eIF5B depletion, ASS1 protein expression was present at only 0.7x that of the control sample in a proteomic analysis performed by Jiang *et al.*[70]

Interestingly, as can be seen in Table W, the metabolite just upstream of fumarate in the citric acid cycle – succinate – is present at greatly depleted numbers in any treatment condition except for my control. However, while this is directly relevant to fumarate levels, I do not see a corresponding change in fumarate under all conditions, and eIF5B depletion does not appear to have a significant effect on succinate levels further than TRAIL already does.

Table 4. metabolite expression set compared to siC samples as 100%

	si-Control	siC + TRAIL	si-eIF5B	si5B + TRAIL
Aspartate	100	87.2	98.0	68.0
Fumarate	100	103.3	109.3	356.0
Succinate	100	51.7	43.7	47.39

While the previously published literature indicates a decrease in ASS1 expression under conditions of eIF5B knockdown, I do notice differential expression of two metabolites on opposite ends of that process.[70] Notably, I do not see a significant change of either metabolite under conditions of eIF5B depletion; further, I was not able to determine relative concentrations of arginosuccinate – the intermediate between aspartate and fumarate. However, while I was not able to observe arginosuccinate, I do see a corresponding decrease in the upstream aspartate as well as an increase in the downstream fumarate, which do agree with one another. As a biproduct of the urea cycle, fumarate also plays an important role in the citric acid cycle (TCA) as an intermediate between succinate and malate. However, through a not-fully-understood interaction, increased levels of fumarate are often associated with increased levels of reactive oxygen species (ROS) and HIF-1 activation.[86]

Fumarate is converted to malate by fumarate hydratase (FH), a newly-identified tumour suppressor in human renal cell carcinomas. Accumulation of fumarate leads to the formation of succinic GSH, a metabolite comprised of fumarate and glutathione. According to Zheng *et al,* chronic succination of GSH can be caused by loss of FH, or by exogenous fumarate.[87] Fumarate has been shown to covalently bind to cysteine residues under physiological conditions through a process known as protein succination. Keap1, an inhibitor of the transcription factor Nrf2, has been shown as a target of protein succination

which leads to the inactivation of Keap1 and subsequent increased activation of Nrf2.[87] Under physiological conditions, Keap1 promotes the ubiquitination of Nrf2, leading to its degradation; however, under conditions of increased fumarate concentration, succination of Keap1 should inhibit its activity, preventing it from promoting the degradation of Nrf2.[87,88] Notably, in our recently published paper on eIF5B depletion in U343, we showed that Nrf2 was greatly downregulated when the cells were depleted of eIF5B and treated with TRAIL.[15] Contrary to this information, I show here that fumarate levels drastically increase only under both eIF5B depletion and TRAIL treatment, a shift that *should* lead to decreased Keap1 activity and therefore greater levels of Nrf2. Succinated glutathione has been shown to increase levels of mitochondrial ROS and HIF-1 activation; however, once again, counter to what we have previously seen, the expected result of this increase in fumarate levels should lead to increased HIF-1 activation – yet, previously unpublished western blots in U343 demonstrate a very significant decrease in HIF1α protein levels under both TRAIL treatment and eIF5B depletion individually, and even greater together. It is quite interesting why both HIF1 and Nrf2 levels both correlate in a direction opposite that of the increased levels of fumarate observed here.[15]

4.1.5 UDP-N-acetylglucosamine

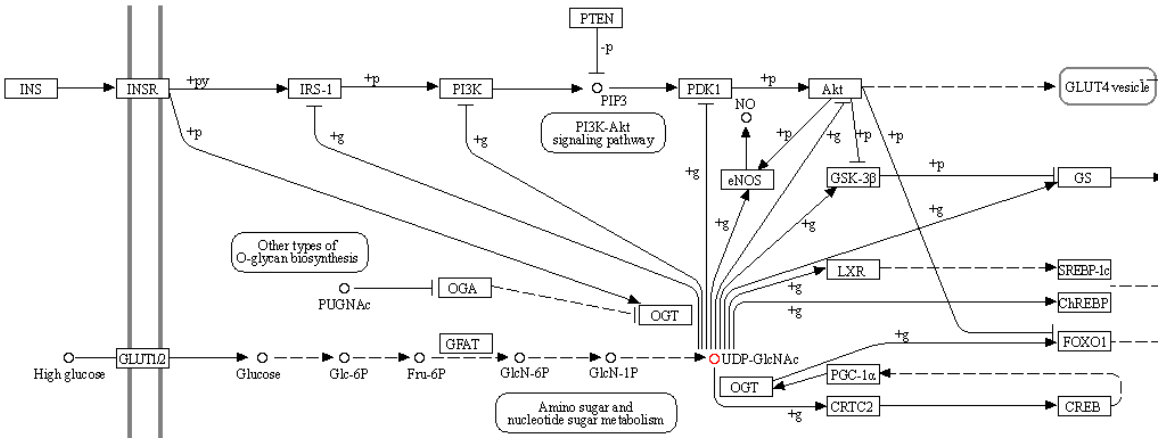

Figure 26. Kegg pathway showing the role and regulation of UDP-GlcNAc. OGT uses UDP-GlcNAc as a substrate for the transfer of GlCNAc onto proteins such as IRS-1, PI3K, PDK1, and CRTC2 which augments their activity.

UDP-N-acetylglucosamine (UDP-GlcNAc) acts as a central hub in the regulation of insulin resistance. Produced through the hexosamine biosynthetic pathway (HBP), UDP-GlcNAc acts as the substrate for O-GlcNAc transferase (OGT) which in turn regulates various pathways by transferring a GlcNAc group onto serine and threonine residues on target proteins.[89] Levels of O-GlcNAcylation are tied tightly to the availability and relative abundance of UDP-GlcNAc. In lymphocytic leukemia cells, overexpression of OGT and subsequent increases in O-GlcNAcylation levels resulted in corresponding increases in the activation of PI3K, Akt, and c-Myc compared to normal B cells. The authors note that this observation is associated with overexpression of HIF-1α and its target glycolytic genes such as lactate dehydrogenase 4 (LDHA). Notably, I saw levels of UDP-GlcNAc decrease with both eIF5B depletion and TRAIL individually, although the concentration of UDP-GlcNAc was not significantly lower in the si-eIF5B+TRAIL treatment condition than the si-C+TRAIL treatment. Jiang *et al* observed a decrease in LDHA protein expression to 0.7x in their eIF5B depleted cells, compared with their control cells.[70] In the same lymphocytic

leukemia cells, when OGT was knocked down, decreases in PI3K and Akt activation were observed – indicating that a decrease in UDP-GlcNAc may be associated with some level of reduction in both PI3K and Akt. Notably, as previously mentioned, we see a very significant decrease in HIF1 protein present under si-eIF5B +TRAIL treatment – this correlates with both the observed LDHA proteomic decreases as well the observed decreases in the OGT substrate UDP-GlcNAc. Ultimately, UDP-GlcNAc and subsequent O-GlcNAcylation levels are heavily involved in cancer biology through promoting glycolysis, proliferation, and invasion through activation of the PI3K/Akt pathway.[89]

4.2 RFA Library Preparation Protocol Establishment and Optimization

One of the objectives of my MSc was establishing and optimizing a protocol for the preparation of RFA libraries. Originally, the optimistic goal was to produce a fully complete library to send off for sequencing and analysis; unfortunately, due to much troubleshooting, delays, and ultimately the COVID-19 university closures, samples did not get sent off for processing. As can be seen in Figure 27, many areas required substantial work to establish and get moving in the development of this pipeline. Almost every step of this pipeline development was done systematically to prevent any avoidable problem before it happened, and yet, multiple times I ran into specific issues which did not repeat themselves when thoroughly investigated. Because some of these issues could not be replicated, I believe that they were due to erroneous handling of the RNA and potential RNAase contamination. I cannot know this for sure, but even under incredible strict working situations with the utmost care, RNAase contamination is quite possible and even quite probable.

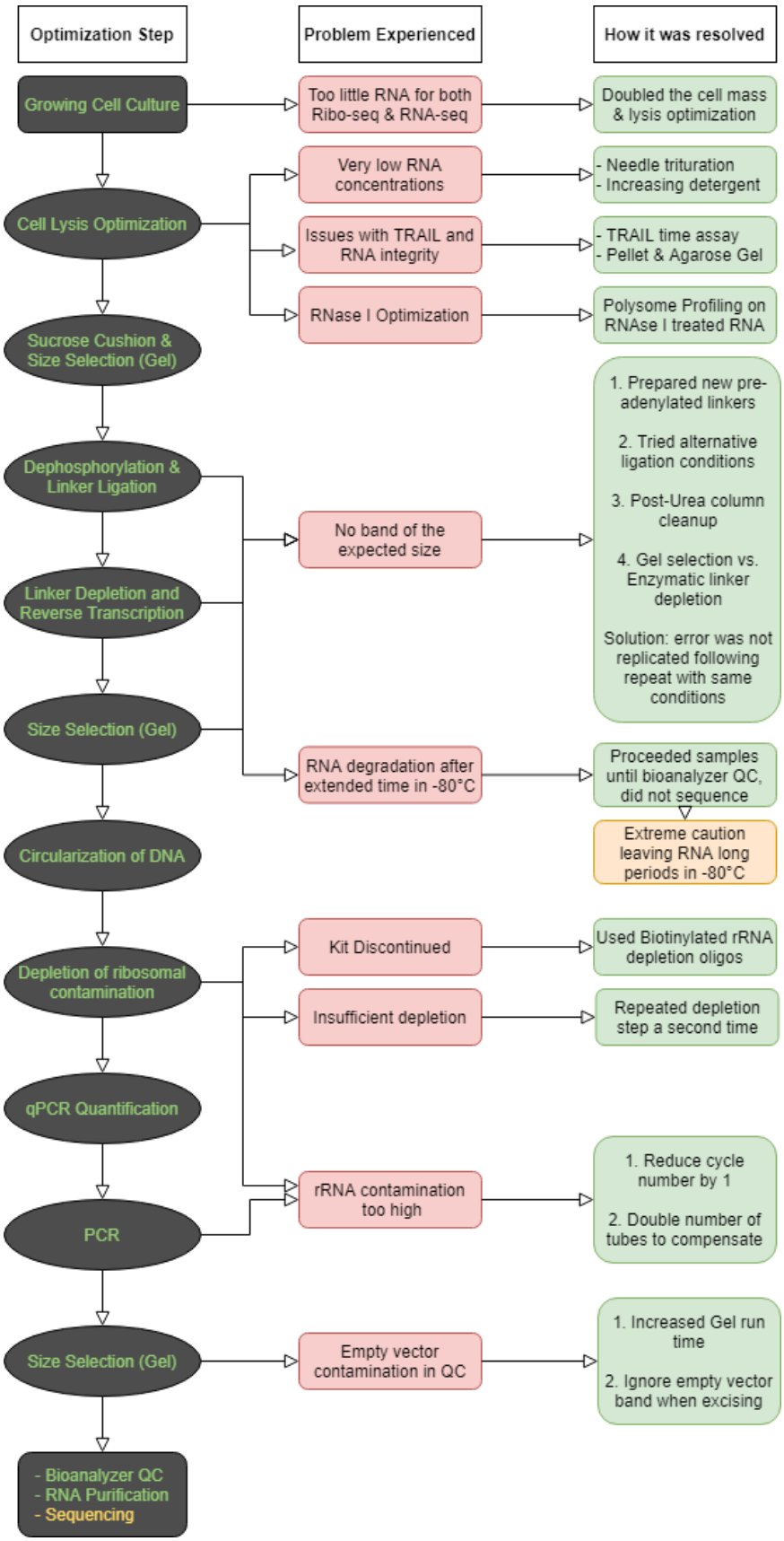

Figure 27. Translatome troubleshooting shown as a flowchart. Steps in the protocol

shown on the left side of the Figure are written in green if they were successfully completed and verified problem-free and yellow if incomplete. Bubbles in the middle of the Figure shown in red summarize issues and problems experienced during the protocol, and bubbles on the right in green explaining how each issue was resolved.

Further, much more work than can be shown in a flowchart went into establishing this protocol on campus. Notably, many weeks of planning went into the development of the specific protocol I used here – I had the opportunity to observe a collaborator perform a variation of this protocol a few years back; however, that protocol was based on the 2012 version of Ingolia *et al*'s ribosome profiling protocol. While there was a lot of overlap between the two protocols, there was also quite a bit of differences, both in reagents, as well as steps taken to make it work with the equipment we had. Almost all of the individual steps in the library preparation protocol were new to me; however, at this time I am confident that even in my absence this protocol could be repeated and completed by another researcher with the resources we have available.

Notably, through the last round of replicates, I successfully solved the issues of low total RNA yield, inadequate isolation of RNA from the lysis buffer, empty vector contaminants in the final library as well as rRNA contamination in the final library. With these problems out of the way, I have successfully completed my objective of establishing a functional and complete protocol for the development of RFA libraries for translatomic analysis. Establishment of this protocol in Dr. Thakor's lab and more generally at the University of Lethbridge will be incredibly important for future project and studies. By developing this multi-omics pipeline I open the opportunity for both my lab as well as future students, faculty, and collaborators to use this technique to bring high throughput analysis to their own projects and experiments. This project was expensive in both time, as

well as laboratory resources; however, having now completed this protocol I am incredibly excited to see future works that come out of both Dr. Thakor's lab as well as the University of Lethbridge.

5 Future Directions

Through this project, I have created opportunity for experimentation as well as opened the door for many new students to take advantage of this technique to further their own studies. If I had more time, there are a few notable experiments that I would like to see ran to further this data. First, I would like to see this protocol repeated and actually sent off for sequencing; with that data available, it would be very interesting to see what sort of enzymes are differentially regulated that cause the observed metabolomic changes. As for direct spin-offs of this project, there are still a few questions that I would like to see explored further:

- Would U343 cells grow in a myo-inositol-free medium under conditions of eIF5B depletion or is the increase in concentration due to increased uptake from the surroundings?
    - My current data does not support a conclusion determining the method by which myo-inositol increases under eIF5B depletion. In performing this experiment, it could be revealed whether this increase is due to increased uptake or increased production.
- Are the different isoforms of Akt regulated differently, or as one collective group?

    - We previously found that total Akt levels appeared unchanged following eIF5B depletion; however, this does not mean that there was not a shift in the balance between all 3 isoforms of Akt. We used an antibody which detected all 3 isoforms. In their 2011 paper, Endersby *et al* demonstrated that tumorigenesis of PTEN null astrocytes was inhibited by depletion of Akt1 or 3, and was accelerated by depletion of Akt2.[90]

- Alongside my metabolomic results, I also froze away aliquots of the medium at time of harvest – this may be useful for to perform 1H NMR on to investigate whether excretion of certain metabolites were affected.
- Do other eukaryotic initiation factors produce similar metabolomic trends to eIF5B, or are my results eIF5B-specific? To assess this, a replicate experiment could be performed using 2 other eIFs in place of eIF5B.
- I would like to see this experiment replicated with a few more GBM lines as well as potentially a few A-II lines. This would be useful to compare whether the observed trend is a U343-specific trend, or rather a GBM / brain cancer-wide trend.
- I would like to see this experiment repeated using 1-5 different time points of TRAIL infection to observe which metabolites change over time as the cell culture gets closer to apoptosis.
- I would like to see this experiment repeated using shRNA knockdown of eIF5B. While this is something that I have attempted in the lab in the past, I generally saw greatly diminished growth rates and they generally lost their

knockdown after a few weeks. Notably, the reason I would like to see this is to observe which metabolites, enzymes, or proteins are responsible for that phenomenon. When using traditional siRNAs as used in this experiment, we do not observe any decreased rate of growth or affect on overall survival in U343 when eIF5B is knocked down. A longer-term knockdown study may provide greater insight into why eIF5B depletion becomes more important the longer the cells are without it.

Finally, I would be extremely interested to see a replicate of this experiment performed on brain tumour initiating stem-like cells (BTIC / BTSC). This would be interesting because these cells have relevance as a transition point to a xenographic mouse tumour model. However, before making that jump, since growing BTIC cell lines are very expensive and time consuming, I believe repeating this experiment with other cell lines would be more advantageous and more in the immediate future.

References

1 Holcik, M. & Sonenberg, N. Translational control in stress and apoptosis. *Nature Reviews. Molecular Cell Biology* **6**, 318-327, doi:http://dx.doi.org/10.1038/nrm1618 (2005).

2 Wang, T. *et al.* Translating mRNAs strongly correlate to proteins in a multivariate manner and their translation ratios are phenotype specific. *Nucleic Acids Research* **41**, 4743-4754, doi:10.1093/nar/gkt178 (2013).

3 J.J *et al.* Systemic Reprogramming of Translation Efficiencies on Oxygen Stimulus. **14**, 1293-1300, doi:10.1016/j.celrep.2016.01.036 (2016).

4 Liu, Y., Beyer, A. & Aebersold, R. On the Dependency of Cellular Protein Levels on mRNA Abundance. *Cell* **165**, 535-550, doi:10.1016/j.cell.2016.03.014 (2016).

5 Ho, J. J. D. *et al.* Oxygen-Sensitive Remodeling of Central Carbon Metabolism by Archaic eIF5B. *Cell Reports* **22**, 17-26, doi:10.1016/j.celrep.2017.12.031 (2018).

6 Sriram, A., Bohlen, J. & Teleman, A. A. Translation acrobatics: how cancer cells exploit alternate modes of translational initiation. *EMBO reports* **19**, e45947, doi:10.15252/embr.201845947 (2018).

7 Thakor, N. & Holcik, M. IRES-mediated translation of cellular messenger RNA operates in eIF2 - independent manner during stress. **40**, 541-552, doi:10.1093/nar/gkr701 (2012).

8 Hinnebusch, A. G., Ivanov, I. P. & Sonenberg, N. Translational control by 5'-untranslated regions of eukaryotic mRNAs. *Science* **352**, 1413-1416, doi:10.1126/science.aad9868 (2016).

9 Ali, I. K., McKendrick, L., Morley, S. J. & Jackson, R. J. Activity of the Hepatitis A Virus IRES Requires Association between the Cap-Binding Translation Initiation Factor (eIF4E) and eIF4G. **75**, 7854-7863, doi:10.1128/jvi.75.17.7854-7863.2001 (2001).

10 Wells, S. E., Hillner, P. E., Vale, R. D. & Sachs, A. B. Circularization of mRNA by Eukaryotic Translation Initiation Factors. **2**, 135-140, doi:10.1016/s1097-2765(00)80122-7 (1998).

11 Weingarten-Gabbay, S. *et al.* Systematic discovery of cap-independent translation sequences in human and viral genomes. *Science* **351**, aad4939, doi:10.1126/science.aad4939 (2016).

12 Godet, A.-C. *et al.* IRES Trans-Acting Factors, Key Actors of the Stress Response. *International Journal of Molecular Sciences* **20**, 924, doi:10.3390/ijms20040924 (2019).

13 Pestova, T. V. *et al.* The joining of ribosomal subunits in eukaryotes requires eIF5B. *Nature* **403**, 332-335, doi:10.1038/35002118 (2000).

14 Yamamoto, H. *et al.* Structure of the mammalian 80S initiation complex with initiation factor 5B on HCV-IRES RNA. **21**, 721-727, doi:10.1038/nsmb.2859 (2014).

15 Ross, J. A. *et al.* Eukaryotic initiation factor 5B (eIF5B) provides a critical cell survival switch to glioblastoma cells via regulation of apoptosis. *Cell Death & Disease* **10**, doi:10.1038/s41419-018-1283-5 (2019).

16 D'Arcy, M. S. Cell death: a review of the major forms of apoptosis, necrosis and autophagy. *Cell Biology International* **43**, 582-592, doi:10.1002/cbin.11137 (2019).

17 Shan, B., Pan, H., Najafov, A. & Yuan, J. Necroptosis in development and diseases. *Genes & Development* **32**, 327-340, doi:10.1101/gad.312561.118 (2018).

18 Xie, Y. *et al.* Ferroptosis: process and function. *Cell Death & Differentiation* **23**, 369-379, doi:10.1038/cdd.2015.158 (2016).

19 Mizushima, N., Levine, B., Cuervo, A. M. & Klionsky, D. J. Autophagy fights disease through cellular self-digestion. *Nature* **451**, 1069-1075, doi:10.1038/nature06639 (2008).

20 Wang, H. *et al.* Mixed Lineage Kinase Domain-like Protein MLKL Causes Necrotic Membrane Disruption upon Phosphorylation by RIP3. *Molecular Cell* **54**, 133-146, doi:10.1016/j.molcel.2014.03.003 (2014).

21 Liu, Y. *et al.* RIP1/RIP3-regulated necroptosis as a target for multifaceted disease therapy (Review). *International Journal of Molecular Medicine*, doi:10.3892/ijmm.2019.4244 (2019).

22 Pistritto, G., Trisciuoglio, D., Ceci, C., Garufi, A. & D'Orazi, G. Apoptosis as anticancer mechanism: function and dysfunction of its modulators and targeted therapeutic strategies. *Aging* **8**, 603-619, doi:10.18632/aging.100934 (2016).

23 Brentnall, M., Rodriguez-Menocal, L., De Guevara, R., Cepero, E. & Boise, L. H. Caspase-9, caspase-3 and caspase-7 have distinct roles during intrinsic apoptosis. *BMC Cell Biology* **14**, 32, doi:10.1186/1471-2121-14-32 (2013).

24 Ghavami, S. *et al.* Apoptosis and cancer: mutations within caspase genes. *Journal of Medical Genetics* **46**, 497-510, doi:10.1136/jmg.2009.066944 (2009).

25 Sadarangani, A. *et al.* TRAIL mediates apoptosis in cancerous but not normal primary cultured cells of the human reproductive tract. *Apoptosis* **12**, 73-85, doi:10.1007/s10495-006-0492-z (2007).

26 Martinon, F. & Tschopp, J. Inflammatory Caspases. *Cell* **117**, 561-574, doi:10.1016/j.cell.2004.05.004 (2004).

27 Kuang, A. A., Diehl, G. E., Zhang, J. & Winoto, A. FADD Is Required for DR4- and DR5-mediated Apoptosis. *Journal of Biological Chemistry* **275**, 25065-25068, doi:10.1074/jbc.c000284200 (2000).

28 Von Karstedt, S., Montinaro, A. & Walczak, H. Exploring the TRAILs less travelled: TRAIL in cancer biology and therapy. *Nature Reviews Cancer* **17**, 352-366, doi:10.1038/nrc.2017.28 (2017).

29 Yuan, X. *et al.* Developing TRAIL/TRAIL death receptor-based cancer therapies. *Cancer and Metastasis Reviews* **37**, 733-748, doi:10.1007/s10555-018-9728-y (2018).

30 Beaudouin, J., Liesche, C., Aschenbrenner, S., Hörner, M. & Eils, R. Caspase-8 cleaves its substrates from the plasma membrane upon CD95-induced apoptosis. *Cell Death & Differentiation* **20**, 599-610, doi:10.1038/cdd.2012.156 (2013).

31 Das, K. K., Shalaby, R. & García-Sáez, A. J. Determinants of BH3 Sequence Specificity for the Disruption of Bcl-xL/cBid Complexes in Membranes. doi:10.1021/acschembio.6b01084 (2017).

32 Bao, Q. & Shi, Y. Apoptosome: a platform for the activation of initiator caspases. *Cell Death & Differentiation* **14**, 56-65, doi:10.1038/sj.cdd.4402028 (2007).

33 Zumbrägel, F. K. *et al.* Survivin does not influence the anti-apoptotic action of XIAP on caspase-9. *Biochemical and Biophysical Research Communications* **482**, 530-535, doi:10.1016/j.bbrc.2016.11.094 (2017).

34 Green, D. R. & Evan, G. I. A matter of life and death. **1**, 19-30, doi:10.1016/s1535-6108(02)00024-7 (2002).

35 Ichim, G. & Tait, S. W. G. A fate worse than death: apoptosis as an oncogenic process. *Nature Reviews Cancer* **16**, 539-548, doi:10.1038/nrc.2016.58 (2016).

36 Graham, K. & Unger, E. Overcoming tumor hypoxia as a barrier to radiotherapy, chemotherapy and immunotherapy in cancer treatment. *International Journal of Nanomedicine* **Volume 13**, 6049-6058, doi:10.2147/ijn.s140462 (2018).

37 Vaux, D. L. Immunopathology of apoptosis ?introduction and overview. *Springer Seminars in Immunopathology* **19**, 271-278, doi:10.1007/bf00787224 (1998).

38 Hassan, M., Watari, H., Abualmaaty, A., Ohba, Y. & Sakuragi, N. Apoptosis and Molecular Targeting Therapy in Cancer. *BioMed Research International* **2014**, 1-23, doi:10.1155/2014/150845 (2014).

39 Amundson, S. A. *et al.* An informatics approach identifying markers of chemosensitivity in human cancer cell lines. *Cancer Res* **60**, 6101-6110 (2000).

40 Twomey, J. & Zhang, B. Circulating Tumor Cells Develop Resistance to TRAIL-Induced Apoptosis Through Autophagic Removal of Death Receptor 5: Evidence from an In Vitro Model. *Cancers* **11**, 94, doi:10.3390/cancers11010094 (2019).

41 Suresh, S. *et al.* eIF5B drives integrated stress response-dependent translation of PD-L1 in lung cancer. *Nat Cancer* **1**, 533-545, doi:10.1038/s43018-020-0056-0 (2020).

42 Wang, J. *et al.* eIF5B gates the transition from translation initiation to elongation. *Nature* **573**, 605-608, doi:10.1038/s41586-019-1561-0 (2019).

43 Wang, J. *et al.* Structural basis for the transition from translation initiation to elongation by an 80S-eIF5B complex. *Nature Communications* **11**, doi:10.1038/s41467-020-18829-3 (2020).

44 Markley, J. L. *et al.* The future of NMR-based metabolomics. *Current Opinion in Biotechnology* **43**, 34-40, doi:10.1016/j.copbio.2016.08.001 (2017).

45 Wishart, D. S. *et al.* HMDB: a knowledgebase for the human metabolome. *Nucleic Acids Research* **37**, D603-D610, doi:10.1093/nar/gkn810 (2009).

46 Laíns, I. *et al.* Metabolomics in the study of retinal health and disease. *Progress in Retinal and Eye Research* **69**, 57-79, doi:10.1016/j.preteyeres.2018.11.002 (2019).

47 Lee, S., Hallis, S. P., Jung, K.-A., Ryu, D. & Kwak, M.-K. Impairment of HIF-1α-mediated metabolic adaption by NRF2-silencing in breast cancer cells. *Redox Biology* **24**, 101210, doi:10.1016/j.redox.2019.101210 (2019).

48 Kumar, R. *et al.* Mitochondrial uncoupling reveals a novel therapeutic opportunity for p53-defective cancers. *Nature Communications* **9**, doi:10.1038/s41467-018-05805-1 (2018).

49 Ingolia, N. T., Brar, G. A., Rouskin, S., McGeachy, A. M. & Weissman, J. S. The ribosome profiling strategy for monitoring translation in vivo by deep sequencing of ribosome-protected mRNA fragments. *Nature Protocols* **7**, 1534-1550, doi:10.1038/nprot.2012.086 (2012).

50 McGlincy, N. J. & Ingolia, N. T. Transcriptome-wide measurement of translation by ribosome profiling. *Methods* **126**, 112-129, doi:10.1016/j.ymeth.2017.05.028 (2017).

51 Bohlen, J. *et al.* DENR promotes translation reinitiation via ribosome recycling to drive expression of oncogenes including ATF4. *Nature Communications* **11**, doi:10.1038/s41467-020-18452-2 (2020).

52 Fernández-Calero, T. *et al.* Fine-tuning the metabolic rewiring and adaptation of translational machinery during an epithelial-mesenchymal transition in breast cancer cells. *Cancer & Metabolism* **8**, doi:10.1186/s40170-020-00216-7 (2020).

53 Anderson, P. E. *et al.* Dynamic adaptive binning: an improved quantification technique for NMR spectroscopic data. *Metabolomics* **7**, 179-190, doi:10.1007/s11306-010-0242-7 (2011).

54 Craig, A., Cloarec, O., Holmes, E., Nicholson, J. K. & Lindon, J. C. Scaling and normalization effects in NMR spectroscopic metabonomic data sets. *Anal Chem* **78**, 2262-2267, doi:10.1021/ac0519312 (2006).

55 Veselkov, K. A. *et al.* Recursive segment-wise peak alignment of biological (1)h NMR spectra for improved metabolic biomarker recovery. *Anal Chem* **81**, 56-66, doi:10.1021/ac8011544 (2009).

56 Goodpaster, A. M., Romick-Rosendale, L. E. & Kennedy, M. A. Statistical significance analysis of nuclear magnetic resonance-based metabonomics data. *Anal Biochem* **401**, 134-143, doi:10.1016/j.ab.2010.02.005 (2010).

57 Wishart, D. S. *et al.* HMDB 4.0: the human metabolome database for 2018. *Nucleic Acids Res* **46**, D608-d617, doi:10.1093/nar/gkx1089 (2018).

58 Frolkis, A. *et al.* SMPDB: The Small Molecule Pathway Database. *Nucleic Acids Res* **38**, D480-487, doi:10.1093/nar/gkp1002 (2010).

59 Chong, J. & Xia, J. Using MetaboAnalyst 4.0 for Metabolomics Data Analysis, Interpretation, and Integration with Other Omics Data. *Methods Mol Biol* **2104**, 337-360, doi:10.1007/978-1-0716-0239-3_17 (2020).

60 Worley, B. & Powers, R. Multivariate Analysis in Metabolomics. *Curr Metabolomics* **1**, 92-107, doi:10.2174/2213235x11301010092 (2013).

61 Kostidis, S., Addie, R. D., Morreau, H., Mayboroda, O. A. & Giera, M. Quantitative NMR analysis of intra- and extracellular metabolism of mammalian cells: A tutorial. *Analytica Chimica Acta* **980**, 1-24, doi:10.1016/j.aca.2017.05.011 (2017).

62 Croze, M. L. & Soulage, C. O. Potential role and therapeutic interests of myo-inositol in metabolic diseases. *Biochimie* **95**, 1811-1827, doi:10.1016/j.biochi.2013.05.011 (2013).

63 Chau, J. F. L., Lee, M. K., Law, J. W. S., Chung, S. K. & Chung, S. S. M. Sodium/myo-inositol cotransporter-1 is essential for the development and function

of the peripheral nerves. *The FASEB Journal* **19**, 1887-1889, doi:10.1096/fj.05-4192fje (2005).

64 Hauser, G. & Finelli, V. N. THE BIOSYNTHESIS OF FREE AND PHOSPHATIDE MYO-INOSITOL FROM GLUCOSE BY MAMMALIAN TISSUE SLICES. *J Biol Chem* **238**, 3224-3228 (1963).

65 Vettukattil, R. *et al.* Differentiating diffuse World Health Organization grade II and IV astrocytomas with ex vivo magnetic resonance spectroscopy. *Neurosurgery* **72**, 186-195; discussion 195, doi:10.1227/NEU.0b013e31827b9c57 (2013).

66 Candiota, A. P., Majós, C. & Julià-Sapé, M. Non-invasive grading of astrocytic tumours from the relative contents of myo-inositol and glycine measured by in vivo mrs. **94**, 319, doi:10.5334/jbr-btr.698 (2011).

67 Broad Institute. *U343_Central_Nervous_System*, <https://portals.broadinstitute.org/ccle/page?cell_line=U343_CENTRAL_NERVOUS_SYSTEM> (2020).

68 Bund, C. *et al.* An integrated genomic and metabolomic approach for defining survival time in adult oligodendrogliomas patients. *Metabolomics* **15**, doi:10.1007/s11306-019-1522-5 (2019).

69 Sanger. *Catalogue Of Somatic Mutations In Cancer (COSMIC)*, <https://cancer.sanger.ac.uk/cell_lines/browse/tissue> (2020).

70 Jiang, X. *et al.* Proteomic Analysis of eIF5B Silencing-Modulated Proteostasis. *PLOS ONE* **11**, e0168387, doi:10.1371/journal.pone.0168387 (2016).

71 Bressler, K. *Elucidating the role of eukaryotic initiation factor 5B (eIF5B) in non-canonical translation initiation* MSc thesis, University of Lethbridge, (2019).

72 Cheng, C. K., Fan, Q. W. & Weiss, W. A. PI3K signaling in glioma--animal models and therapeutic challenges. *Brain Pathol* **19**, 112-120, doi:10.1111/j.1750-3639.2008.00233.x (2009).

73 Ségaliny, A. I., Tellez-Gabriel, M., Heymann, M. F. & Heymann, D. Receptor tyrosine kinases: Characterisation, mechanism of action and therapeutic interests for bone cancers. *J Bone Oncol* **4**, 1-12, doi:10.1016/j.jbo.2015.01.001 (2015).

74 Bressler, K. *et al.* Depletion of eukaryotic initiation factor 5B (eIF5B) reprograms the cellular transcriptome and leads to activation of endoplasmic reticulum (ER) stress and c-Jun N-terminal Kinase (JNK). *Cell Stress and Chaperones* **(In press)** (2020).

75 Clague, M. J., Urbé, S. & de Lartigue, J. Phosphoinositides and the endocytic pathway. *Exp Cell Res* **315**, 1627-1631, doi:10.1016/j.yexcr.2008.10.005 (2009).

76 Misra, S., Miller, G. J. & Hurley, J. H. Recognizing Phosphatidylinositol 3-Phosphate. *Cell* **107**, 559-562, doi:10.1016/s0092-8674(01)00594-3 (2001).

77 Zhong, Q. *et al.* Endosomal localization and function of sorting nexin 1. *Proc Natl Acad Sci U S A* **99**, 6767-6772, doi:10.1073/pnas.092142699 (2002).

78 Miura, S. *et al.* Hgs (Hrs), a FYVE domain protein, is involved in Smad signaling through cooperation with SARA. *Mol Cell Biol* **20**, 9346-9355, doi:10.1128/mcb.20.24.9346-9355.2000 (2000).

79 Sun, Y., Hedman, A. C., Tan, X., Schill, N. J. & Anderson, R. A. Endosomal type Iγ PIP 5-kinase controls EGF receptor lysosomal sorting. *Dev Cell* **25**, 144-155, doi:10.1016/j.devcel.2013.03.010 (2013).

80 Rodgers, S. J., Ferguson, D. T., Mitchell, C. A. & Ooms, L. M. Regulation of PI3K effector signalling in cancer by the phosphoinositide phosphatases. *Bioscience Reports* **37**, doi:10.1042/bsr20160432 (2017).

81 Kurmi, K. *et al.* Tyrosine Phosphorylation of Mitochondrial Creatine Kinase 1 Enhances a Druggable Tumor Energy Shuttle Pathway. *Cell Metab* **28**, 833-847.e838, doi:10.1016/j.cmet.2018.08.008 (2018).

82 Glunde, K., Bhujwalla, Z. M. & Ronen, S. M. Choline metabolism in malignant transformation. *Nat Rev Cancer* **11**, 835-848, doi:10.1038/nrc3162 (2011).

83 Tessier, A. G., Yahya, A., Larocque, M., Fallone, B. G. & Syme, A. Sci-Fri PM: Delivery - 09: Response of a tumor xenograft model to radiation therapy using magnetic resonance spectroscopy. *Med Phys* **39**, 4644, doi:10.1118/1.4740204 (2012).

84 Li, Y., Ji, F., Jiang, Y., Zhao, T. & Xu, C. Correlation analysis of expressions of PTEN and p53 with the value obtained by magnetic resonance spectroscopy and apparent diffusion coefficient in the tumor and the tumor-adjacent area in magnetic resonance imaging for glioblastoma. *J buon* **23**, 391-397 (2018).

85 Miyake, T. & Parsons, S. J. Functional interactions between Choline kinase α, epidermal growth factor receptor and c-Src in breast cancer cell proliferation. *Oncogene* **31**, 1431-1441, doi:10.1038/onc.2011.332 (2012).

86 Sullivan, L. B. *et al.* The proto-oncometabolite fumarate binds glutathione to amplify ROS-dependent signaling. *Mol Cell* **51**, 236-248, doi:10.1016/j.molcel.2013.05.003 (2013).

87 Zheng, L. *et al.* Fumarate induces redox-dependent senescence by modifying glutathione metabolism. *Nat Commun* **6**, 6001, doi:10.1038/ncomms7001 (2015).

88 Deshmukh, P., Unni, S., Krishnappa, G. & Padmanabhan, B. The Keap1-Nrf2 pathway: promising therapeutic target to counteract ROS-mediated damage in

cancers and neurodegenerative diseases. *Biophys Rev* **9**, 41-56, doi:10.1007/s12551-016-0244-4 (2017).

89 Very, N., Vercoutter-Edouart, A. S., Lefebvre, T., Hardivillé, S. & El Yazidi-Belkoura, I. Cross-Dysregulation of O-GlcNAcylation and PI3K/AKT/mTOR Axis in Human Chronic Diseases. *Front Endocrinol (Lausanne)* **9**, 602, doi:10.3389/fendo.2018.00602 (2018).

90 Endersby, R., Zhu, X., Hay, N., Ellison, D. W. & Baker, S. J. Nonredundant Functions for Akt Isoforms in Astrocyte Growth and Gliomagenesis in an Orthotopic Transplantation Model. *Cancer Research* **71**, 4106-4116, doi:10.1158/0008-5472.can-10-3597 (2011).